Baroclinic nonlinear saturation and secondary instability of current-undercurrent meanders

Xianliang Chen,[1] Jianping Gan,[1,*] and James C. McWilliams[2]

[1]*Center for Ocean Research in Hong Kong and Macau, Department of Mathematics, and Department of Ocean Science, The Hong Kong University of Science and Technology, Hong Kong, People's Republic of China*

[2]*Department of Atmospheric and Oceanic Sciences, University of California, Los Angeles, Los Angeles, California, USA*

(Received 3 July 2024; accepted 5 September 2024; published 7 October 2024)

This work studies the nonlinear formation and secondary instability of jet meanders due to baroclinic instability. The continuously stratified current-undercurrent system in the Western Pacific Ocean is extracted as an idealized model problem. Two-dimensional linear eigenmode analysis identifies surface (upper) and subsurface (lower) amplified baroclinic modes for the two currents, respectively. A weakly nonlinear instability framework is developed to resolve the temporal evolution of the most unstable eigenmode, its smaller-scale harmonics and the mean flow distortion under the quasigeostrophic scaling. After initial rapid amplification, these modes reach amplitude saturation and phase locking due to nonlinear interaction. The saturation of the upper mode results in upper-current meanders, whereas it can split the undercurrent into multiple cores. In comparison, the saturation of the lower mode leads to undercurrent meanders, which drive deeper waters to flow in the undercurrent direction but negligibly affect the upper layer. The two saturation states succumb to modest secondary instability, which is identified through a Floquet-based secondary instability analysis for a fully three-dimensional shape function. The fundamental resonance is found to dominate the upper-mode case, where the perturbation takes the form of mesoscale cyclones and anticyclones. Conversely, significant detuned resonance is identified for the lower-mode case, which quickly induces aperiodic motions in terms of the meanders. Implications for realistic oceanic flows are also discussed.

DOI: 10.1103/PhysRevFluids.9.103801

I. INTRODUCTION

Oceanic flows cover an extremely vast range of temporal and spatial scales, but most of the kinetic energy resides in mesoscale eddies [1], whose characteristic scales are ∼10–100 km in the horizontal. A large portion of these eddies are initially formed by baroclinic instability (BCI), which extracts available potential energy from vertically sheared mean fields. Therefore, BCI has long been one of the central problems in geophysical fluid dynamics [2]. The linear mechanisms of BCI are generally well understood. The CSP (after Charney and Stern [3] and Pedlosky [4]) necessary condition was summarized for inviscid zonal flows, which judges BCI based on the sign change of the potential vorticity (PV) gradient of the basic flow. Furthermore, Smith [5] (also Feng *et al.* [6]) processed realistic profiles to show that virtually the entire ocean is baroclinically unstable. They also provided a view of how different types of BCIs were distributed globally. The linear instability problem is designed for infinitesimal perturbations, whereas nonlinearity becomes nonignorable

*Contact author: magan@ust.hk

after the perturbation grows to a finite amplitude [7]. In fact, Chelton *et al.* [8] demonstrated that essentially all the observed mesoscale eddies in global oceans were nonlinear. Compared to the linear problem, the nonlinear mechanism of BCI is more complicated and less well understood.

Weakly nonlinear theories for BCI were first developed based on perturbation expansions around the point of marginal instability. Pedlosky [9,10] analyzed the interaction between a baroclinic wave and the mean zonal flow in a quasigeostrophic (QG) model for one-dimensional (1D) basic flow, and revealed that the equilibrated finite-amplitude state exhibits an oscillation when excluding dissipation. Meanwhile, the eddy-induced fluxes can reduce the mean vertical shear, hence stabilizing the baroclinic system [11,12]. Although 1D basic flow (usually zonal on a β plane) serves as an ideal theoretical model, cross-stream variation of the basic flow, e.g., in a jet flow, is ubiquitous in realistic oceans. The perturbation evolution in the latter system involves an interplay between baroclinic and barotropic instabilities, where a mechanism of baroclinic growth and barotropic decay was revealed by Simmons and Hoskins [13] using the primitive equations (PEs). Moreover, the nonlinear BCI, coupled with barotropic and topographic effects sometimes, can lead to flow meanders and eddy detachment [14–16]. Such a mechanism is successful in explaining the current meanders widely observed in a number of regions, including the Gulf Stream [17–19], Antarctic Circumpolar Current [20], Kuroshio Current (KC) [21], and Brazil Current system [22]. The along-current wavelength of the meanders was shown to well match the most unstable baroclinic mode [22,23], suggesting its dominant role in the initially linear growth regime. Meanwhile, harmonics of the unstable baroclinic modes rapidly grow due to nonlinearity, which distorts the mean flow and excites smaller-scale motions [15,24,25].

The primary methodology in these works on nonlinear meanders is directly solving the QG equations or PEs in the physical space. This is powerful because of the capability to incorporate strong nonlinearity, complex topography, multiple scales, and other factors. On the other hand, it can be interesting, from the theoretical perspective, to develop a nonlinear instability framework, which solves the linearized equations for each perturbation mode and its harmonics with nonlinear terms as the forcing. Such a framework is less applicable to realistic flows, but it can help understand modal interactions and be efficient when only several leading modes dominate the system, thus providing guidance for reduced-order modeling and to explore the underlying physics. This thought has been adopted (e.g., Pedlosky [10]) for 1D basic flows, but is less explored in two-dimensional (2D) or more complex flows such as the jet flow meanders. Developing such a nonlinear analysis framework for baroclinic meanders is one of the central tasks of this work.

There are two more interesting points regarding baroclinic meanders of currents. The first point is whether the meander can be stably sustained, which constitutes a secondary instability problem in the sense that the formation of meanders through nonlinear BCI is the primary instability. It is observed in some numerical simulations that mesoscale eddies can be generated and pinched off the meanders [15,18], but they are not directly related to the instability of meanders through systematic instability analysis. On the other hand, a baroclinic meandering jet as the basic flow is inhomogeneous in all three spatial directions (and even temporarily varying), so the secondary instability analysis (SIA) requires a three-dimensional (3D) shape function with extremely high computational cost. By assuming periodicity in the along-current and temporal directions, the Floquet theory can simplify the system to some extent [26,27]. However, the final eigenvalue problem is still essentially three dimensional, which, in the language of global instability [28], is a triglobal problem: the final discretized matrix for the eigenvalue computation is of dimensions $(N_x \times N_y \times N_z)^2$ with $N_{x,y,z}$ the grid numbers. Though requiring huge computational cost, 3D SIA is valuable to obtain an overall understanding of the instability of baroclinic meanders over a large wavenumber space. Therefore, realizing 3D Floquet-based SIA for the present continuously stratified system is another objective of this work, targeted for the baroclinic meanders obtained from the above nonlinear instability framework.

The second interesting point is the effect of upper-layer current meanders on deep waters. For example, Donohue *et al.* [29] reported observationally that deep eddy kinetic energy experienced a marked increase coincident with the growth of upper-layer meanders. Ikeda [15] also noted that

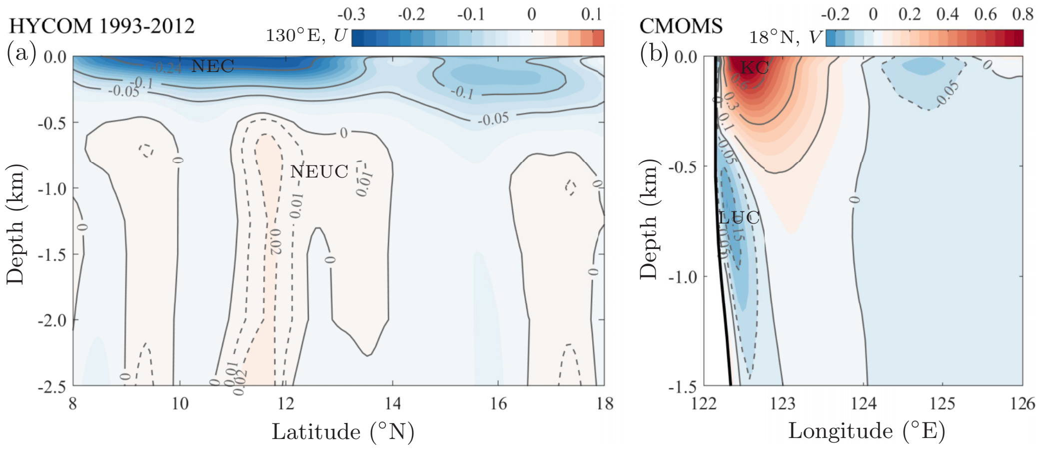

FIG. 1. Annual mean cross section of the (a) zonal velocity (m/s) at 130 °E [using the Hybrid Coordinate Ocean Model (HYCOM) data [32]), and (b) meridional velocity (m/s) at 18 °N from the China Sea multiscale ocean modeling system (CMOMS) [31,33]. NEC, North Equatorial Current; NEUC, North Equatorial Undercurrent; KC, Kuroshio Current; and LUC, Luzon Undercurrent.

though the upper-layer meanders kept moving eastward like the initial field, the lower-layer water could move westward except for the regions near the layer center. This interaction between layers becomes more interesting in the presence of an undercurrent, which is the focus of this work. The two currents flowing in opposite directions are expected to experience baroclinic meanders separately, whereas their linear and nonlinear interactions can possibly reshape each other. The current-undercurrent system widely exists in global oceans, and plays crucial roles in subsurface circulation. Some well-known examples are the eastward Equatorial Undercurrent, and the undercurrent system in the Western Pacific Ocean (WPO) [30]. Figure 1 illustrates two different forms of undercurrents in the WPO. The first example is the North Equatorial Current (NEC) and North Equatorial Undercurrent (NEUC) taking the form of isolated jets away from lateral boundaries. The second example is the KC–Luzon Undercurrent (LUC) system acting as western boundary currents. Currently, the dynamics of these undercurrents are not fully understood. It is believed that barotropic and baroclinic instabilities have joint contributions, and the latter is crucial in the formation and maintenance of the undercurrent system [31]. Therefore, the present work extracts an idealized model from the WPO undercurrent system, to further understand the dynamics and current-undercurrent interaction due to intrinsic BCI.

We start from a smooth basic flow (horizontal scale ∼300 km and depth ∼2000 m), obtained from the annual mean results of the China Sea multiscale ocean modeling system (CMOMS) developed in the present authors' group for the WPO and marginal seas [33,34]. The basic flow is subject to two types of BCIs, and the two most unstable eigenmodes are separately initiated. The perturbation grows linearly and then nonlinearly to form the baroclinic meanders for the current and undercurrent, respectively. A saturation state is finally reached, which succumbs to different types of secondary instabilities, leading to the formation of aperiodic smaller-scale (still mesoscale) motions. We adopt a continuously stratified QG model for this problem, whose justification will be presented in later sections. The value of this work is in three aspects. First, we develop a weakly nonlinear framework to track the temporal evolution of the perturbation mode, its harmonics, and the along-stream mean flow, which benefits the interpretation of modal interactions and reduced-order modeling. Second, we develop a Floquet-based secondary instability framework to analyze the instability of the saturated meanders, which is a full 3D instability (triglobal) calculation scarcely explored before. Third, we intend to reveal the unique interaction between the current and undercurrent due to nonlinear and secondary instabilities. The remaining parts are organized as follows.

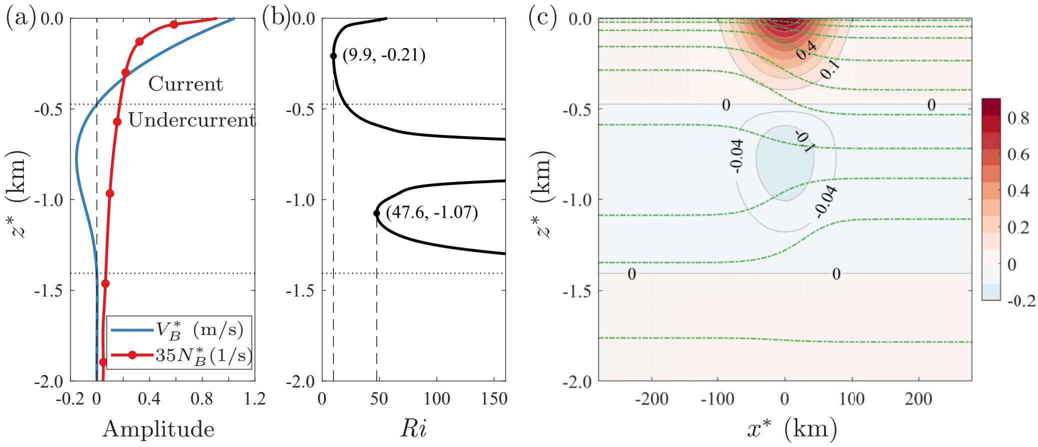

FIG. 2. Basic flow distribution: vertical profiles of (a) the meridional velocity and buoyancy frequency, (b) the Richardson number at the jet center ($x = 0$), and (c) the contours of the meridional velocity (m/s) and buoyancy (green lines).

Section II describes the problem setup, and the formulation of nonlinear and secondary instability analyses. Section III presents the linear eigenmode results, which provide the parameter ranges for subsequent nonlinear calculations. The effects of non-normality and inertial gravity waves are also discussed. Afterwards, the nonlinear and secondary instability results are discussed in Secs. IV and V, respectively. The work is finally summarized in Sec. VI.

II. PROBLEM FORMULATIONS

A. Flow setup and governing equations

As mentioned in Sec. I, we extract an idealized current-undercurrent model from the WPO to study the role of intrinsic instability. Therefore, a periodic channel is configured to exclude the effects of topography. The two currents are modeled as jets, whose initial basic state is assumed geostrophic and meridionally uniform (justified later). Specifically, the basic stream function is $\Psi_B = \Psi_B(x, z)$, the zonal and meridional velocities are $U_B = 0$, $V_B = V_B(x, z)$, and the buoyancy field is $B_B = B_B(x, z)$, where x and z are the zonal and vertical coordinates. We take two steps to construct the basic flow. First, we obtain the jet centerline profile $V^*_{B,1\mathrm{D}}(z^*)$ and $N_B^{2*}(z^*)$ from the CMOMS, as shown in Fig. 2(a). Here, N_B is the buoyancy frequency and the superscript $*$ denotes dimensional variables. The upper-layer current (depth less than 470 m) flows northward with the peak velocity at the surface. The subsurface undercurrent flows southward, whose maximum velocity amplitude is 0.15 m/s at depth 780 m; this location is termed the undercurrent core hereafter. In the second step, a jetlike flow is formulated as $V_B^*(x^*, z^*) = V^*_{B,1\mathrm{D}}(z^*)\exp[-(x^* - X_c^*)^2/X_W^{2*}]$, where $X_c^* = 0$ is the location of the jet center and X_W^* is the jet half-width. As a practical measure, the width $2X_W^*$ is set to 130 km. The resulting basic flow is displayed in Fig. 2(c), where the buoyancy field (isopycnals) is built upon the thermal-wind relation $f^*\partial V_B^*/\partial z^* = \partial B_B^*/\partial x^*$, $f^* = f_0^* + \beta^* y^*$ is the Coriolis frequency, and $\beta^* = \partial f^*/\partial y^*$. The computational domain spans 560 km in the zonal direction, and is truncated at depth 2000 m, where V_B^* drops to zero.

The geostrophy of the basic flow is evaluated using the Richardson and vorticity Rossby numbers,

$$\mathrm{Ri} = \frac{N^{*2}}{(\partial U^*/\partial z^*)^2 + (\partial V^*/\partial z^*)^2}, \quad \mathrm{Ro}_\zeta = \frac{\zeta^*}{f^*} = \frac{1}{f^*}\left(\frac{\partial V^*}{\partial x^*} - \frac{\partial U^*}{\partial y^*}\right), \tag{1}$$

where the subscript ζ is to distinguish from the Ro used for later nondimensionalization. These two parameters also measure the strength of vertical and horizontal shears, respectively. The Ri

TABLE I. Dimensional parameters for the present case.

Latitude	L_0^* (km)	H_0^* (m)	U_0^* (m/s)	t_0^* (day)	N_0^* (1/s)	w_0^* (mm/s)	C_H^* (m^2/s)
18 °N	111.2	2000	1.000	1.287	2.505×10^{-3}	3.589	10.00

distribution at the jet center is shown in Fig. 2(b). The minimum Ri is 9.9 in the upper layer, so balanced baroclinic modes are anticipated to dominate over other types [35]. In the undercurrent region, Ri is higher (more geostrophic) and tends to infinity around the undercurrent core with minimal vertical shear. In terms of Ro_ζ, it is less than 0.05 in the undercurrent region, and reaches its maximum 0.29 at the surface where the horizontal shear intensifies. The temporal evolution of Ri and Ro_ζ will be monitored when the basic flow is disturbed due to instability.

Considering the relatively large scale of the flow and the ranges of Ri and Ro_ζ, we adopt a QG model, as widely considered before for baroclinic jet and meander problems at similar scales [25,36–38]. The surface mixed layer is thus not modeled. Comparison with a linear PE model will be presented in Sec. III to demonstrate the minor role of inertial waves during linear transient growth. For the nonlinear regime, Spall and Robinson [18] noted, in their cases of Gulf Stream meanders, that both the QG and PE models reproduced the major dynamic events, which is the main concern here, whereas ageostrophic advection in the PE model contributed to reproduce more realistic ring structures. Analogous conclusions were reached by Klein *et al.* [39] and Zurita-Gotor and Vallis [40] for nonlinear BCI problems. More discussions on this point will be presented in Sec. VI.

The central variable in the QG model is the stream function ψ; then $u^* = -\partial\psi^*/\partial y^*$, $v^* = \partial\psi^*/\partial x^*$, and $b^* = f^*\partial\psi^*/\partial z^*$. For numerical convenience, we introduce the following nondimensionalization:

$$(x, y) = \frac{(x^*, y^*)}{L_0^*}, \quad z = \frac{z^*}{H_0^*}, \quad t = \frac{t^* U_0^*}{L_0^*} = \frac{t^*}{t_0^*}, \quad f = \frac{f^*}{f_0^*} = f_0 + \beta y, \quad N = \frac{N^*}{N_0^*},$$
$$\psi = \frac{\psi^*}{U_0^* L_0^*}, \quad (u, v) = \frac{(u^*, v^*)}{U_0^*}, \quad w = \frac{w^* \bar{N}^{*2} H_0^*}{f_0^* U_0^{*2}} = \frac{w^*}{w_0^*}, \quad b = \frac{b^* H_0^*}{f_0^* U_0^* L_0^*}. \tag{2}$$

Here, L_0^* and H_0^* are the horizontal and vertical length scales such that $z \in [-1, 0]$, U_0^* and N_0^* are the reference velocity and buoyancy frequency, and w is the vertical velocity. As a result, the nondimensional PV is

$$q = \beta y + \Delta_h \psi + \frac{f_0^2}{\mathrm{Bu}}\frac{\partial}{\partial z}\left(\frac{1}{\bar{N}^2}\frac{\partial \psi}{\partial z}\right), \quad \mathrm{Bu} = \frac{\mathrm{Ro}^2}{\mathrm{Fr}^2} = \frac{\bar{N}_0^{*2} H_0^{*2}}{L_0^{*2} f_0^{*2}}, \tag{3}$$

where $\Delta_h = \partial^2/\partial x^2 + \partial^2/\partial y^2$, $\bar{N}(z)$ is the horizontally averaged buoyancy frequency under the QG scaling, and Bu and Fr are the Burger and Froude numbers. The computational parameters are summarized in Table I; N_0^* is determined as listed so that $\mathrm{Bu} = 1$.

We consider a rigid-lid vertical boundary, i.e., $w = 0$ at $z = -1, 0$, so the nondimensional QG equation takes the form of

$$\frac{\partial q}{\partial t} + u\frac{\partial q}{\partial x} + v\frac{\partial q}{\partial y} = \mathscr{F}_q + \mathscr{D}_q, \quad -1 < z < 0,$$
$$\frac{\partial b}{\partial t} + u\frac{\partial b}{\partial x} + v\frac{\partial b}{\partial y} = \mathscr{F}_b + \mathscr{D}_b, \quad z = -1, 0, \tag{4}$$

where $\mathscr{F}$ and $\mathscr{D}$ represent the forcing and dissipation terms. For the present periodic channel setup, the relaxational restoring force is the most widely used form of forcing, which can be regarded as a highly idealized parametrization for large-scale unresolved processes that maintain the flow (or the factors that form the current like the upstream effects) [38–41]. The restoring force thus acts to pull the flow back to the prescribed basic state in Fig. 2, as $\mathscr{F}_q = -r_R(q - Q_B)$ and $\mathscr{F}_b = -r_R(b - B_B)$, where the crucial parameter r_R is defined as the restoring rate. As will be shown in Sec. IV, the restoring force is significant in the present model for the formation of saturated meanders. The dissipation term contains explicit diffusion (coefficient C_H) posed in the numerical model (CMOMS), and small-scale mixing (e.g., Ref. [25], coefficient $C_D = 10^{-7}$) for numerical stability, as $\mathscr{D}_q = C_H \Delta_h q - C_D \Delta_h^2 q$. The dissipation coefficients for b are related through a unity Prandtl number. The dissipation effects will be quantified through the energy budget analysis (Sec. II D). For later use, Eq. (4) is expressed in an operator form as $\mathscr{Q}(\psi) = 0$.

B. Nonlinear instability analysis

To analyze the perturbation behavior, we decompose the field into the basic part and the perturbed part, $\psi(x,y,z,t) = \Psi_B(x,z) + \psi'(x,y,z,t)$. From Eq. (4), the linearized perturbation equation around the basic state is $\mathscr{Q}(\Psi_B + \psi') - \mathscr{Q}(\Psi_B) = 0$, which is explicitly written as

$$\begin{aligned}
\frac{\partial q'}{\partial t} &= -\left[\left(V_B \frac{\partial}{\partial y} + r_R - C_H \Delta_h + C_D \Delta_h^2\right) q' + Q_{B,x} u' + \beta v'\right] \\
&\quad - \left(u' \frac{\partial q'}{\partial x} + v' \frac{\partial q'}{\partial y}\right), \quad \text{for } -1 < z < 0 \\
\frac{\partial b'}{\partial t} &= -\left[\left(V_B \frac{\partial}{\partial y} + r_R - C_H \Delta_h + C_D \Delta_h^2\right) b' + f_0 V_{B,z} u'\right] \\
&\quad - \left(u' \frac{\partial b'}{\partial x} + v' \frac{\partial b'}{\partial y}\right), \quad \text{for } z = -1, 0,
\end{aligned} \tag{5}$$

where $Q_{B,x}$ is the zonal gradient of Q_B and $V_{B,z}$ is the vertical shear. The β effect is shown to have a minor influence on the modes and length scales of interest (detailed in Appendix B), so a simpler f plane is further assumed, which enables a zonally periodic boundary condition to simplify the treatment of high-order horizontal boundary conditions introduced by dissipation. Equation (5) is written in an operator form in terms of ψ' as $\mathbf{B}\partial\boldsymbol{\psi}'/\partial t = \mathbf{C}\boldsymbol{\psi}' + \mathbf{F}'$, where $\mathbf{B}$ and $\mathbf{C}$ are linear operators, $\boldsymbol{\psi}'$ is the global vector containing all the variables, and $\mathbf{F}'$ denotes the eddy-induced nonlinear term.

In the Fourier space, ψ' is decomposed in the meridional direction as

$$\psi'(x,y,z,t) = \sum_{m=-M}^{M} \hat{\psi}'_m(x,z,t) \exp(\mathrm{i} m k_y y), \tag{6}$$

where M is the truncation order, $\hat{\psi}'_m$ is the shape function, and k_y is the fundamental meridional wavenumber. Since the volume transport of a current is often of particular interest, we introduce the notation $\bar{\psi}' = \Psi_B + \hat{\psi}'_0$ for the meridionally mean field averaged over one fundamental wavelength $L_y = 2\pi/k_y$. From Eq. (5), the governing equation for each Fourier component ($m = -M, \ldots, M$) is

$$\frac{\partial}{\partial t}\hat{\boldsymbol{\psi}}'_m = \mathbf{L}_m \hat{\boldsymbol{\psi}}'_m + \hat{\mathbf{N}}'_m, \quad \text{where } \mathbf{L}_m \equiv \mathbf{B}_m^{-1}\mathbf{C}_m, \quad \hat{\mathbf{N}}'_m \equiv \mathbf{B}_m^{-1}\hat{\mathbf{F}}'_m. \tag{7}$$

Here, $\hat{\mathbf{F}}'_m$ is the Fourier component of $\mathbf{F}'$ obtained after a convolution operation. A symmetry $\hat{\psi}'_{-m} = \hat{\psi}'^{\dagger}_m$ exists, where $\dagger$ denotes complex conjugate.

Following the procedures in Sec. I, we first consider linear eigenmodes for infinitesimal perturbations. A temporal stability problem is established after expanding the temporal derivatives using a factor $\exp(-\mathrm{i}\omega t)$ and neglecting the nonlinear terms. The modes of different m are hence decoupled, and the resulting complex eigenvalue problem is $\mathbf{L}\hat{\psi}' = -\mathrm{i}\omega\hat{\psi}'$. The real and imaginary parts of the eigenvalue, ω_r and ω_i, represent the frequency and growth rate, respectively. This is a 2D, or biglobal, stability problem (e.g., Ref. [42]) since the eigenfunction is 2D (x, z). The non-normality of $\mathbf{L}$ may play a role in the perturbation transient growth [43], which will be discussed in Sec. III.

Next, we discuss the weakly nonlinear problem. If the basic flow is uniform across the stream (zonal here; $X_W \to \infty$), then the most unstable eigenmode is the strict solution to Eq. (7) under negligible viscous dissipation. In other words, the eigenmode can linearly grow regardless of its amplitude, since the nonlinear term keeps absent ($\hat{\mathbf{N}}'_m = 0$, due to $v' = \partial/\partial x = 0$). This is the setup of Pedlosky [26] and Radko *et al.* [44] to study the secondary BCI. Due to the zonal variation of V_B in the present case, $\mathbf{N}'$ is not zero and introduces nonlinear effects during the linear amplification of the fundamental mode ($m = 1$). Since $\mathbf{F}'$ is quadratic, harmonic modes mk_y ($m = 0, 2, 3, \dots$) are generated. The $|m| > 1$ modes have shorter length scales than the fundamental one, while the $m = 0$ mode serves as a modification to the meridionally mean flow, which is termed the meridionally mean flow distortion (MFD) mode. Thereby, we can construct a set of nonlinear equations for $\hat{\psi}'_m$ based on Eq. (7), to obtain the temporal evolution of different modes.

Through further inspection, $\hat{\psi}'_m$ varies temporarily in both amplitudes and shapes. The complex amplitude part behaves as an oscillatory wave which grows or decays exponentially. Therefore, we introduce a regularity condition, inspired by the spatial nonlinear instability problems [45]. This condition enables more physical interpretation of the modes' evolution, and also reduces the numerical stiffness of the nonlinear equations. Specifically, $\hat{\psi}'_m$ is decomposed as

$$\hat{\psi}'_m(x, z, t) = \hat{\Psi}'_m(x, z, t)\mathcal{A}_m(t), \qquad \text{where } \mathcal{A}_m(t) \equiv \exp\left[-\mathrm{i}\int_0^t \omega_m(t)\mathrm{d}t\right]. \tag{8}$$

The amplification of $\hat{\psi}'_m$ can be absorbed in the amplitude function $\mathcal{A}_m$, to make $|\hat{\Psi}'_m|$ slowly vary with time using a closure condition specified later. Combining Eqs. (7) and (8) leads to the equation for $\hat{\Psi}'_m$ as

$$\frac{\partial \hat{\mathbf{\Psi}}'_m}{\partial t} = (\mathbf{L}_m + \mathrm{i}\omega_m \mathbf{I})\hat{\mathbf{\Psi}}'_m + \frac{\hat{\mathbf{N}}'_m}{\mathcal{A}_m}, \tag{9}$$

where $\mathbf{I}$ is the identity matrix. For practical use, a norm is required to measure the amplitude of $\hat{\psi}'_m$ (or $\hat{\Psi}'_m$). A natural choice is the energy norm, comprised of the perturbation kinetic energy (KE, $\hat{K}'_m$) and (available) potential energy ($\hat{P}'_m$), as

$$\hat{E}'_m(t) = \frac{1}{2}\|\hat{\Psi}'_m\|_E = \frac{1}{2}\iint_\Omega \left(\hat{u}'^{\dagger}_m\hat{u}'_m + \hat{v}'^{\dagger}_m\hat{v}'_m + \frac{f_0}{\mathrm{Bu}}\frac{\hat{b}'^{\dagger}_m\hat{b}'_m}{\bar{N}^2}\right)\mathrm{d}x\mathrm{d}z = \hat{K}'_m + \hat{P}'_m, \tag{10}$$

where Ω stands for the whole domain. Note that u'_m, v'_m and b'_m in Eq. (10) are obtained from $\hat{\Psi}'_m$ (hereinafter) rather than $\hat{\psi}'_m$. The energy norms for $\hat{\psi}'_m$ and $\hat{\Psi}'_m$ differ by a factor $\mathcal{A}^\dagger_m\mathcal{A}_m$, i.e., $\hat{e}'_m = \|\hat{\psi}'_m\|_E/2 = \mathcal{A}^\dagger_m\mathcal{A}_m\hat{E}'_m$. The algorithm details regarding the inner and outer iterations are listed in Appendix A.

Regarding the numerics, both the Chebyshev collocation points and high-order finite difference schemes can be used in the vertical direction. The former scheme requires fewer grids to reach grid independence, but using the latter can save considerable memory and computational cost for the triglobal SIA (next section) at equivalent accuracy [46]. Thereby, the fourth-order finite difference scheme is used, and more points are clustered near the surface due to the larger gradients there. Moreover, Fourier spectral methods are adopted in the zonal direction. For the MFD mode, the discretized Eq. (9) is singular since an arbitrary constant can be added to $\hat{\Psi}'_0$ with the equation satisfied. Though its derivatives $\hat{u}'_0$, $\hat{v}'_0$, and $\hat{b}'_0$ are unaffected by the constant, we supplement one auxiliary boundary condition, $\int \hat{\Psi}'_0\,\mathrm{d}x = 0$ at $z = 0$, for mathematical well-posedness [7]. Besides, a relaxation technique analogous to that by Zhao *et al.* [47] is adopted for $|\hat{N}'_m|$ to enhance robustness.

Notably, Eq. (9) is linearized around the initial basic state Ψ_B, not the temporally varying mean state $\bar{\psi}'$, so $\mathbf{L}_m$ remains unchanged during the temporal marching, which is numerically convenient. To fully validate this treatment of linearization and the above nonlinear framework, we also implement a solver for directly solving Eq. (4) in the physical space, which is termed fully nonlinear simulation (FNS). The spectral methods are employed in all three spatial directions [48]: the Fourier discretization in the horizontal and the Chebyshev method in the vertical. Time stepping is realized through a third-order Runge-Kutta scheme. Comparison between the FNS and nonlinear instability results will be presented in Sec. IV.

C. Secondary instability analysis

The flow driven by the primary instability will reach saturation ($|\hat{\psi}'_m|$ nearly unvaried, or $\omega_{m,i} \approx 0$; see Sec. IV). It is of interest to study whether the meridionally periodic saturation state is stable, i.e., whether the saturation can be sustained. Therefore, SIA is introduced to study the stability of the primary saturation [26,49–52].

The new basic flow of interest is from Eqs. (6) and (8), taking the form of

$$\widetilde{\psi}'(x,y,z,t) = \Psi_B + \sum_{m=-M}^{M} \hat{\Psi}'_m \exp\left(\mathrm{i}mk_y y - \mathrm{i}\int_0^t \omega_m\,\mathrm{d}t\right). \tag{11}$$

The secondary instability perturbation ψ''_s satisfies $\mathscr{Q}(\widetilde{\psi}' + \psi''_s) - \mathscr{Q}(\widetilde{\psi}') = 0$ (the operator $\mathscr{Q}$ is defined in Sec. II A). Since we are concerned with normal modes, the nonlinear terms of ψ''_s are dropped, and the linear governing equation for ψ''_s is

$$\begin{aligned}
&\frac{\partial q''_s}{\partial t} + \tilde{u}'\frac{\partial q''_s}{\partial x} + \tilde{v}'\frac{\partial q''_s}{\partial y} + \frac{\partial \tilde{q}'}{\partial x}u''_s + \frac{\partial \tilde{q}'}{\partial y}v''_s = -r_R q''_s + C_H\Delta_h q''_s - C_D\Delta_h^2 q''_s, \qquad \text{for } -1 < z < 0\\
&\frac{\partial b''_s}{\partial t} + \tilde{u}'\frac{\partial b''_s}{\partial x} + \tilde{v}'\frac{\partial b''_s}{\partial y} + \frac{\partial \tilde{b}'}{\partial x}u''_s + \frac{\partial \tilde{b}'}{\partial y}v''_s = -r_R b''_s + C_H\Delta_h b''_s - C_D\Delta_h^2 b''_s, \qquad \text{for } z = -1, 0.
\end{aligned} \tag{12}$$

Compared with Eq. (5), zonal velocity and the meridional derivatives of the basic flow are present. Meanwhile, Eqs. (12) cannot be directly solved as in Sec. II B, because the basic-flow coefficients additionally vary with t and y.

Fortunately, the following two observations regarding the saturation state in the present model help make ψ''_s solvable. First, for a moment t_s during the saturation regime, the amplitude variation of $\widetilde{\psi}'$ around t_s is negligible considering the minimal primary growth rates $\omega_{m,i} \approx 0$. As will be shown later, the growth rates of different primary instability modes in the saturation regime can be one order of magnitude lower than those of the secondary instability modes, making this "slowly varying" condition valid. Second, it is found that at saturation, the fundamental and harmonic modes have nearly the same phase velocities, i.e., $c_{r,m} \approx c_{r,1} = \omega_{r,1}/k_y$. As a result, Eq. (11) can be written, after some simple algebra, as

$$\widetilde{\psi}'(x,y,z,t;t_s) = \Psi_B + \sum_{m=-M}^{M} G_m(t_s)\hat{\Psi}'_m(x,z;t_s)\exp[\mathrm{i}mk_y(y - c_r t)], \tag{13}$$

where the complex amplitude is $G_m(t_s) = \exp(-\mathrm{i}\int_0^{t_s}\omega_m\,\mathrm{d}t + \mathrm{i}\omega_{m,r}t_s)$, and the subscript 1 in $c_{r,1}$ or $\omega_{r,1}$ is omitted. Notably, G_m and $\hat{\Psi}'_m$ are independent of y and t, so $\widetilde{\psi}'$ is periodic in terms of a reference coordinate $y_c = y - c_r t$, i.e., $\widetilde{\psi}'(x, y_c + \lambda_y, z; t_s) = \widetilde{\psi}'(x, y_c, z; t_s)$. Mathematically, the differential equation with periodic coefficients can be solved through the Floquet theory; for more details, one can refer to Herbert [53] and Wolfe and Samelson [54]. Consequently, the solution for the temporal SIA takes the form of

$$\psi''_s(x,y,z,t) = \exp(\sigma_s t)\sum_{m=-M_s}^{M_s} \hat{\psi}''_{s,m}(x,z)\exp[\mathrm{i}(m+\varepsilon_d)(k_y y - \omega_r t)]. \tag{14}$$

Here, $\sigma_s = \sigma_{s,r} + \mathrm{i}\sigma_{s,i}$ is the characteristic exponent, $\sigma_{s,r}$ is the mode growth rate, and $\sigma_{s,i}$ is the shift in circular frequency relative to ω_r; M_s is the truncated order, not necessarily equal to M in Eq. (13); $\hat{\psi}''_{s,m}$ is the shape function; and ε_d is the detuning parameter, representing the differences in wavelength and frequency between the secondary basic flow and modal fluctuations. For a converged series, Eq. (14) gives identical results when ε_d is varied by an integer, so we only need to consider $-0.5 < \varepsilon_d \leqslant 0.5$. The criteria to truncate Eq. (14) will be discussed in Sec. V. According to the wavenumber relation between $\widetilde{\psi}'$ and ψ''_s, the secondary instability modes can be classified into three types [53], namely, the fundamental ($\varepsilon_d = 0$), subharmonic ($\varepsilon_d = 0.5$), and detuned (other ε_d) types. In particular, the detuned resonance is responsible for inducing the perturbation aperiodic in terms of $\widetilde{\psi}'$ and continuous in spectra, but this mechanism is rarely explored in previous geophysical applications.

After substituting Eqs. (13) and (14) into Eq. (12), we arrive at a generalized eigenvalue problem for σ_s in an operator form as

$$\hat{\mathbf{B}}'\frac{\partial}{\partial t}\hat{\boldsymbol{\psi}}''_s - \hat{\mathbf{C}}'\hat{\boldsymbol{\psi}}''_s = \mathbf{0}, \quad \rightarrow \quad \sigma_s\hat{\mathbf{B}}'\hat{\boldsymbol{\psi}}''_s = [\hat{\mathbf{C}}' + \mathrm{i}(m+\varepsilon_d)\omega_r\hat{\mathbf{B}}']\hat{\boldsymbol{\psi}}''_s. \tag{15}$$

Here, the global matrices $\hat{\mathbf{B}}'$ and $\hat{\mathbf{C}}'$ are related to $\widetilde{\psi}'$, k_y, ω_r, and ε_d. Since $\widetilde{\psi}'$ and ψ''_s are both expanded in series, their product in Eq. (12) involves a convolution, so the equations for $\hat{\psi}''_{s,m}$ ($m = -M_s, \dots, M_s$) cannot be decoupled. Therefore, the global vector $\hat{\boldsymbol{\psi}}''_s = [\hat{\psi}''_{s,-M_s}, \dots, \hat{\psi}''_{s,M_s}]^{\mathrm{T}}$ contains all the perturbation shape functions, and the matrix dimension in Eq. (15) is up to $(N_x \times N_y \times N_z)^2$, where $N_y = 2M_s$ for the subharmonic type and $N_y = 2M_s + 1$ for the other two types (see Ref. [53] for details). Consequently, Eq. (15) represents a full 3D, or triglobal, instability problem of extremely high computational cost. In oceanic applications, such 3D instability calculations were realized by Wolfe and Samelson [54], Berloff *et al.* [49], and Shevchenko *et al.* [55] for two- or three-layer QG models, whereas it has been scarcely explored before in continuously stratified flows as in the present case. For the sake of affordability, only a set of (∼10–20) discrete eigenmodes of leading growth rates, instead of the whole spectrum, are solved. The Krylov-Shur algorithm is employed to reduce the cost [56]. The SIA solver is verified through an atmospheric Eady-type case studied by Stevens and Hakim [57], as detailed in Appendix B.

D. Energy budget analysis

The energy budget analysis is frequently employed to provide insights into flow dynamics. The diagnostic budgets for KE and potential energy are readily obtained from the perturbation vorticity ($\zeta = \Delta_h\psi$) and buoyancy equations for the primary and secondary instabilities, respectively. For the primary instability, the budget equations for KE, potential energy, and total energy (TE) after spatial integral are written as

$$\frac{\partial \hat{K}'_m}{\partial t} + 2\omega_{m,i}\hat{K}'_m = \overbrace{-2r_R\hat{K}'_m}^{\text{Restoring}} + \overbrace{\langle -V_{B,x}\mathrm{Re}(\hat{v}'^{\dagger}_m\hat{u}'_m)\rangle}^{\text{Barotropic}}$$
$$+ \underbrace{\frac{1}{\mathrm{Bu}}\langle \mathrm{Re}(\hat{b}'^{\dagger}_m\hat{w}'_m)\rangle}_{\text{Buoyancy flux}} + \underbrace{\langle \mathrm{Re}(\hat{\Psi}'^{\dagger}_m\mathscr{D}'_{\zeta,m})\rangle}_{\text{Dissipation}} + \underbrace{\langle \mathrm{Re}(-\hat{\Psi}'^{\dagger}_m\mathbf{F}'_{\zeta,m}/\mathcal{A}_m)\rangle}_{\text{Nonlinear}}, \tag{16a}$$

$$\frac{\partial \hat{P}'_m}{\partial t} + 2\omega_{m,i}\hat{P}'_m = \overbrace{-2r_R\hat{P}'_m}^{\text{Restoring}} + \overbrace{\frac{f_0}{\mathrm{Bu}}\left\langle -\frac{V_{B,z}}{\bar{N}^2}\mathrm{Re}(\hat{b}'^{\dagger}_m\hat{u}'_m)\right\rangle}^{\text{Baroclinic}}$$
$$- \underbrace{\frac{1}{\mathrm{Bu}}\langle \mathrm{Re}(\hat{b}'^{\dagger}_m\hat{w}'_m)\rangle}_{\text{Buoyancy flux}} + \underbrace{\frac{1}{\mathrm{Bu}}\left\langle \frac{1}{\bar{N}^2}\mathrm{Re}(\hat{b}'^{\dagger}_m\mathscr{D}'_{b,m})\right\rangle}_{\text{Dissipation}} + \underbrace{\frac{1}{\mathrm{Bu}}\left\langle \frac{1}{\bar{N}^2}\mathrm{Re}(\hat{b}'^{\dagger}_m\mathbf{F}'_{b,m}/\mathcal{A}_m)\right\rangle}_{\text{Nonlinear}}, \tag{16b}$$

$$\frac{\partial \hat{E}'_m}{\partial t} + 2\omega_{m,i}\hat{E}'_m = \overbrace{-2r_R\hat{E}'_m}^{\text{Restoring}} + \overbrace{\langle -V_{B,x}\mathrm{Re}(\hat{v}'^{\dagger}_m\hat{u}'_m)\rangle}^{\text{Barotropic}} + \underbrace{\frac{f_0}{\mathrm{Bu}}\left\langle -\frac{V_{B,z}}{\bar{N}^2}\mathrm{Re}(\hat{b}'^{\dagger}_m\hat{u}'_m)\right\rangle}_{\text{Baroclinic}} + \underbrace{\langle \mathrm{Re}(\hat{\Psi}'^{\dagger}_m\mathscr{D}'_{q,m})\rangle}_{\text{Dissipation}} + \underbrace{\langle \mathrm{Re}(\hat{\Psi}'^{\dagger}_m\mathbf{F}'_{q,m}/\mathcal{A}_m)\rangle}_{\text{Nonlinear}}, \tag{16c}$$

where $\mathrm{Re}(\cdot)$ denotes the real part of complex, and $\langle\cdot\rangle$ is the volume integral as in Eq. (10). Note that the pressure work term $(f_0/\mathrm{Bu})\langle\partial\mathrm{Re}(\hat{\Psi}'^{\dagger}_m\hat{w}'_m)/\partial z\rangle$ is zero subject to the rigid-lid boundary condition; also, the integrated contribution of the β effect is zero. The physical meanings of each term are labeled accordingly, reflecting the contributions from the restoring force (RF), barotropic (BT), baroclinic (BC), dissipation (DP), and nonlinear (NL) components. The BT and BC terms stand for direct energy transfers between the basic flow and the perturbation, while NL describes interscale transfers. Besides, the buoyancy flux (BF) term represents the energy transfer between KE and potential energy, which is canceled out in Eq. (16c).

The left-hand sides of Eqs. (16) represent the temporal growth rates measured by KE, potential energy, and TE, respectively, so Eqs. (16) suggest a decomposition of the perturbation growth rate [58]. Taking Eq. (16c) as an example, the growth rate measured by $\|\hat{\psi}'_m\|_E^{1/2}$ and the growth rate contribution of, e.g., the barotropic components are

$$\chi_{E,m} = \omega_{m,i} + \frac{1}{\sqrt{\hat{E}'_m}}\frac{\partial\sqrt{\hat{E}'_m}}{\partial t} = \omega_{m,i} + \frac{1}{2\hat{E}'_m}\frac{\partial \hat{E}'_m}{\partial t}, \quad \text{and} \quad \chi_{E,\mathrm{BT},m} = -\frac{1}{2\hat{E}'_m}\langle V_{B,x}\mathrm{Re}(\hat{v}'^{\dagger}_m\hat{u}'_m)\rangle, \tag{17}$$

respectively. The contributions of other terms are defined likewise. Consequently, the contribution of each physical process to the perturbation growth is quantified.

The energy budget equations for the secondary instability perturbations can be similarly derived as in Eqs. (16). The energy norm now takes the form of

$$E''_s = \frac{1}{2}\|\psi''_s\|_E = \frac{1}{2}\exp(2\sigma_{s,r}t)\sum_m\iint_\Omega\left(\hat{u}''^{\dagger}_{s,m}\hat{u}''_{s,m} + \hat{v}''^{\dagger}_{s,m}\hat{v}''_{s,m} + \frac{f_0}{\mathrm{Bu}}\frac{\hat{b}''^{\dagger}_{s,m}\hat{b}''_{s,m}}{\bar{N}^2}\right)\mathrm{d}x\mathrm{d}z, \tag{18}$$

and the budget equation for the total energy is

$$\begin{aligned} 2\sigma_{s,r}E''_s &= \overbrace{-2r_RE''_s}^{\text{Restoring}} + \overbrace{\langle\mathrm{Re}(\mathscr{T}''_s)\rangle}^{\text{Barotropic}} + \overbrace{\langle\mathrm{Re}(\mathscr{C}''_s)\rangle}^{\text{Baroclinic}} + \overbrace{\langle\mathrm{Re}(\psi''^{\dagger}_s\mathscr{D}''_{q,s})\rangle}^{\text{Dissipation}}, \\ \mathscr{T}''_s &= -\left[\left(\frac{\partial\tilde{u}'}{\partial x} - \frac{\partial\tilde{v}'}{\partial y}\right)\frac{u''^{\dagger}_s u''_s - v''^{\dagger}_s v''_s}{2} + \left(\frac{\partial\tilde{u}'}{\partial y} + \frac{\partial\tilde{v}'}{\partial x}\right)v''^{\dagger}_s u''_s\right], \\ \mathscr{C}''_s &= -\frac{f_0 b''^{\dagger}_s}{\mathrm{Bu}\bar{N}^2}\left(\frac{\partial\tilde{v}'}{\partial z}u''_s - \frac{\partial\tilde{u}'}{\partial z}v''_s\right). \end{aligned} \tag{19}$$

The budget equations for KE and potential energy, and the growth-rate decomposition as in Eq. (17), can be similarly defined.

III. LINEAR EIGENMODE RESULTS

The linear eigenmode is computed first to determine the dominant perturbation mode, which provides the parameter ranges for subsequent nonlinear calculations. A grid convergence study suggests a mesh $N_x \times N_z = 64\times101$ to obtain grid-independent results. Two primary unstable modes are identified, whose growth rates and phase velocities are plotted in Fig. 3 as functions of k_y ($r_R = 0$). Other modes of relatively low growth rates (gray lines) will not be considered hereafter. The mode amplified in the upper layer is termed the upper mode. It propagates northward

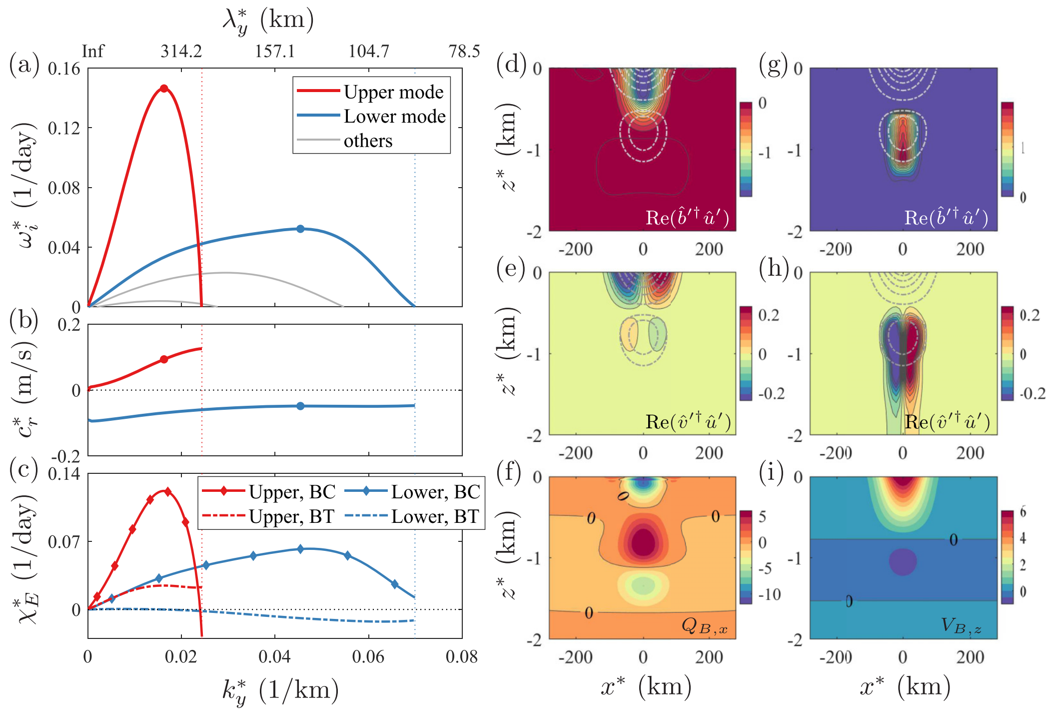

FIG. 3. Linear eigenmode results: (a) growth rates, (b) phase velocities, and (c) energy budgets of the upper and lower modes, and the contours of [(d), (g)] $\mathrm{Re}(\hat{b}'^{\dagger}\hat{u}')$ and [(e), (h)] $\mathrm{Re}(\hat{v}'^{\dagger}\hat{u}')$ for the most unstable [(d), (e)] upper ($k_y^* = 0.016\,\mathrm{km}^{-1}$) and [(g), (h)] lower ($0.046\,\mathrm{km}^{-1}$) modes, respectively. The grey dashed lines in the right-hand panels denote the basic velocity. Panels (f) and (i) are the contours of $Q_{B,x}$ and $V_{B,z}$ for reference, where x and z denote partial derivatives as in Sec. II.

($c_r > 0$), resides in the relatively long wave region ($\lambda_y^* > 250\,\mathrm{km}$), and reaches the highest growth rate among other modes. In comparison, the lower mode amplifies in the undercurrent region, and propagates southward in line with the basic flow. It is active at a shorter wavelength than the upper one, consistent with the local higher Ri according to the Eady scaling [35].

The growth rates are decomposed in Fig. 3(c) to classify different modes. The viscous dissipation term contributes negligibly ($<3\times10^{-4}\,\mathrm{day}^{-1}$) to the total growth for both modes, and hence is not shown. The barotropic component is mildly destabilizing for the upper mode, and slightly stabilizes the lower mode. In comparison, the baroclinic component is the dominant one for both the upper and lower modes, implying that they two are primarily baroclinic modes. These baroclinic modes can be further classified based on the behavior of the mean PV, according to the CSP condition. As a result, the surface-amplified upper mode is of the Charney type, where $Q_{B,x}$ and $V_{B,z}$ have opposite signs at the surface [see Figs. 3(f) and 3(i)]. The subsurface lower mode is of the Phillips type, where $Q_{B,x}$ changes sign in the interior. The spatial distributions of BC and BT for the most unstable upper and lower modes are also displayed in Fig. 3. The baroclinic component, as reflected from the horizontal buoyancy flux $\mathrm{Re}(\hat{b}'^{\dagger}\hat{u}')$, is mainly distributed around the jet center where the vertical shear is the strongest. In comparison, the barotropic part, reflected from the Reynolds stress $\mathrm{Re}(\hat{v}'^{\dagger}\hat{u}')$, is located at the jet flanks with pronounced horizontal shear.

In addition to baroclinic modes, inertial modes such as inertial gravity waves (IGWs, also known as Poincaré waves) may play a role in the perturbation evolution, but they are excluded in the QG model. Therefore, the linear PE model, as detailed in Appendix C, is also solved to distinguish the effects of inertial modes, and justify the usage of the QG model. Note that we consider the 1D basic

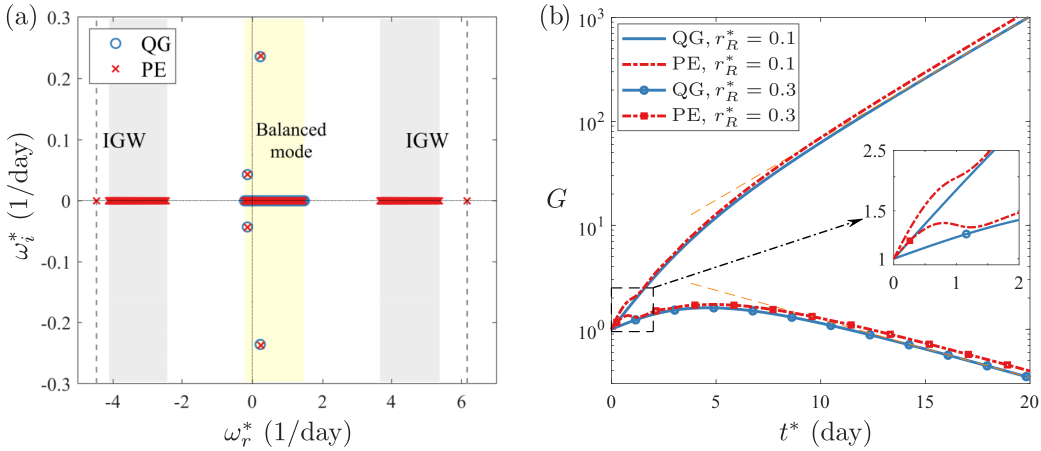

FIG. 4. (a) Global eigenmode spectrum ($r_R = 0$) and (b) the energy amplification factors in TGA at different r_R^* (day^{-1}) by the QG and PE models ($k_y^* = 0.016\,\mathrm{km}^{-1}$). The orange dashed lines in panel (b) are the upper eigenmode results from QG. The basic flow for this figure is the 1D profile in Fig. 2(a) with $k_x = 0$.

flow in Fig. 2(a) for Fig. 4, which will be explained later. First, the mode spectra are compared in Fig. 4(a) between the two models, at $k_y^* = 0.016\,\mathrm{km}^{-1}$ when the baroclinic mode in Fig. 3 is the most unstable (zero zonal wavenumber k_x). Neutral and non-neutral balanced modes appear in the range $\min V_B \leqslant \omega_r/k_y \leqslant \max V_B$, and the eigenvalues from the QG equations well match those from PE, as expected from the relatively large $\mathrm{Ri} \gg 1$ [35]. Besides the balanced modes, two branches of neutral IGWs are present in the PE model. A rough estimation of their wavenumber ranges is [59]

$$\omega_r = k_y V_B \pm (1/\mathrm{Ro})\sqrt{f^2 + \mathrm{Bu} N_B^2 \left(k_x^2 + k_y^2\right)/k_z^2}, \tag{20}$$

where k_z is a virtual vertical wavenumber introduced to make the perturbation equation solvable. As shown in Fig. 4(a), Eq. (20) in the $k_z \to \infty$ limit well predicts the frequency ranges of the IGWs.

Though neutral, IGWs may affect the perturbation evolution through non-normality and modal interaction with balanced modes. To quantify the collective contributions of these IGWs to the perturbation linear growth, we adopt the transient growth analysis (TGA) [43], which solves a linear initial value problem $G(t; k_x, k_z) = \max_t(\|\check{\psi}'(t)\|_E/\|\check{\psi}'(0)\|_E)$ considering all the eigenmodes; G is the energy amplification ratio and $\check{\psi}'$ is a linear combination of all the eigenmodes. TGA requires an accurate resolution of all eigenmodes, so a dense mesh $N_z = 301$ is needed for the present case to obtain grid-independent TGA results. Since the whole spectrum is required, only the 1D basic flow at $x = 0$ is considered in Fig. 4 for numerical affordability, which can at least partially serve our purpose. The TGA results of the QG and PE models are shown in Fig. 4(b) at two r_R, which are selected so that the perturbation is asymptotically unstable and stable, respectively. For the two r_R cases, G grows faster than the most unstable eigenmode before day 13, suggesting mild transient growth due to modal linear interactions. Regarding the effects of IGWs, the QG and PE models give nearly identical G after day 2. The IGWs indeed lead to a higher energy growth at the initial moment (PE results), but they rapidly decay within the first one or two days. This is consistent with the results of Heifetz and Farrell [60], and is ascribed to the fact that the IGWs are nearly perpendicular to the balanced modes at high Ri. Therefore, we conclude that the unstable baroclinic upper and lower modes, well described by the QG model, dominate the linear temporal evolution of the perturbation.

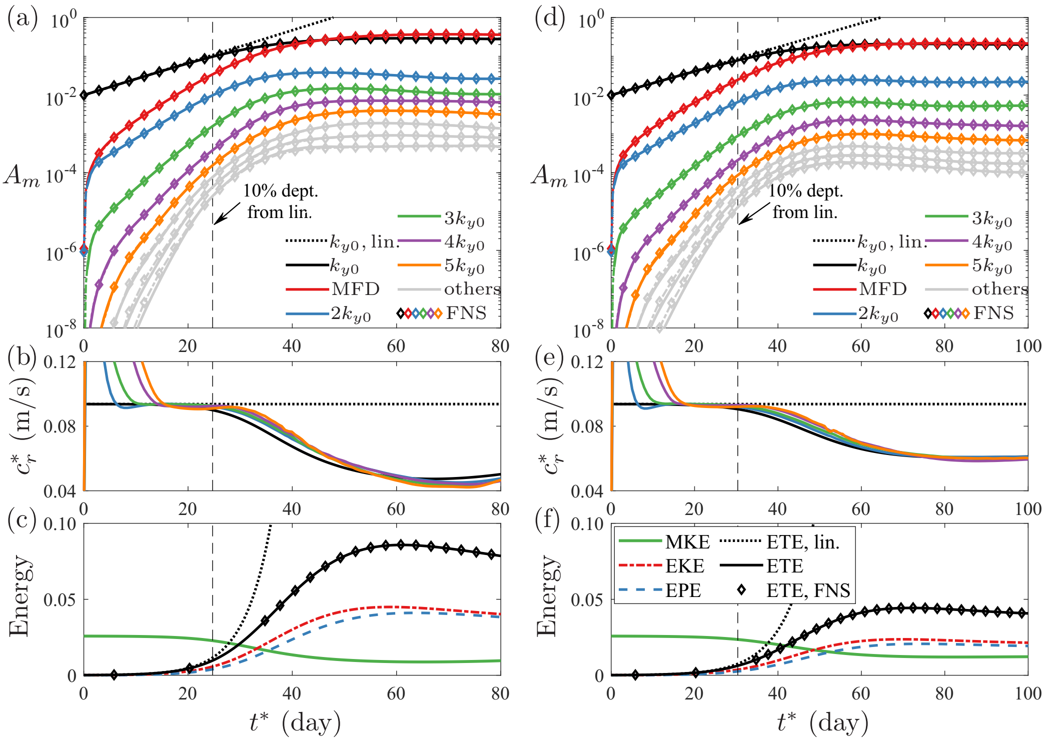

FIG. 5. Upper-mode cases: temporal evolution of the [(a), (d)] amplitudes and [(b), (e)] phase velocities of different Fourier modes, and the [(c), (f)] mean and eddy energies. Panels (a), (b), (d), and (e) share the same legends, and so do panels (c) and (f). Panels (a)–(c) are for the $r_R^* = 0.050\,\mathrm{day}^{-1}$ case, and panels (d)–(f) are for $0.075\,\mathrm{day}^{-1}$. The linear (lin.) instability results are also shown in dotted lines for reference.

IV. NONLINEAR INSTABILITY AND SATURATION

Nonlinear interactions come into play when the perturbation is linearly amplified to a certain value. Since the linear growth is exponential, the most unstable mode in Fig. 3 is more likely to dominate the linear regime. Therefore, we focus on the nonlinear growth of the most unstable upper and lower modes. Notably, it is highly idealized that the initiated perturbation is monochromatic in terms of k_y; it is inevitably broadband with random noise. Nevertheless, the present idealized model can be insightful for studying modal interactions and represents a universal formation mechanism of meanders and smaller-scale motions.

A. Upper-mode case

The upper-mode case is studied first, and three representative values $r_R^* = 0.050$, 0.075, and $0.10\,\mathrm{day}^{-1}$ are selected. The initial perturbation is the $k_{y0}^* = 0.016\,\mathrm{km}^{-1}$ upper mode obtained from Sec. III. Its initial amplitude $A_1(0) = [\|\hat{\psi}_1'(0)\|]^{1/2}$ is set to 1% for all cases to allow linear growth initially, where the subscript 1 denotes the fundamental mode $k_y = k_{y0}$. The harmonic modes mk_{y0} ($m = 0, 2, 3, \ldots$) are later generated by the nonlinear forcing and are rapidly amplified, as shown in Fig. 5(a). The amplitude of the fundamental mode (A_1) deviates from its linear trace by 10% at day 25 and starts to saturate. After day 45, A_1 only slightly varies and remains around 0.3. Other harmonic modes have similar experiences of first rapid growth and then saturation. The MFD mode ($k_y = 0$) reaches a comparable amplitude with the fundamental mode, suggesting severe distortion of the meridionally mean flow. In comparison, the modes $2k_{y0}$, $3k_{y0}$, $\ldots$, have increasingly low

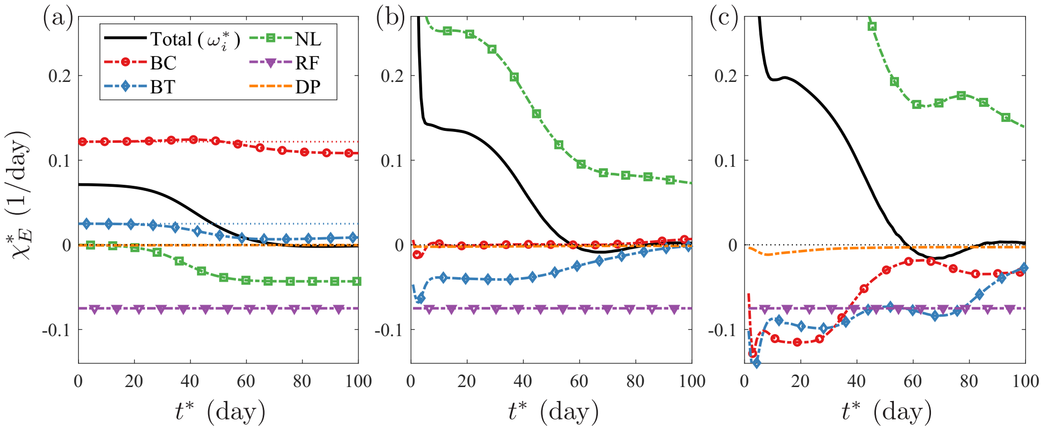

FIG. 6. Growth-rate decomposition based on TE for the (a) fundamental, (b) $k_y = 2k_{y0}$, and (c) $k_y = 3k_{y0}$ modes in the upper-mode $r_R^* = 0.075\,\mathrm{day}^{-1}$ case. The dotted lines in panel (a) are the linear reference. The term notations are defined in Sec. II D, repeated here as BC, baroclinic; BT, barotropic; NL, nonlinear; RF, restoring force; and DP, dissipation.

amplitudes in the saturation regime, and $A_{m\geqslant 2}$ are at least one order of magnitude smaller than A_1 and A_0. This is beneficial to construct a simple model considering only three or four modes to well represent the process in Fig. 5, as will be discussed in Sec. IV C. To fully verify the nonlinear instability results, the FNS solver is employed on an $N_x \times N_y \times N_z = 80\times 80\times 101$ mesh to run the QG simulation from the same initial field at $t = 0$. As shown in Fig. 5, the temporal evolution of A_m from FNS is in perfect agreement with the nonlinear instability analysis, demonstrating the reliability and accuracy of the latter method.

The temporal evolution of the perturbation total energy $e' = \sum_{m\neq 0} \hat{e}'_m$, termed eddy TE (ETE) here, is plotted in Fig. 5(c), along with the kinetic and potential parts. Accordingly, the kinetic energy of the meridionally mean flow $\bar{\psi}'$ is termed MKE here. It is observed that EKE quickly surpasses MKE, and the three eddy energies all slowly decrease in the saturation regime. A nearly equal partitioning between EKE and EPE is reached throughout because the horizontal scale of the basic flow is comparable with the baroclinic deformation radius [61]. In fact, the saturation of the eddy energies due to nonlinear BCI is a universal mechanism [23,24,39].

Another variable of interest is the phase velocity of different modes, as displayed in Fig. 5(b). Due to nonlinear interactions, $c_{r,1}$ is lowered by up to 50% in the saturation regime, compared to its linear counterpart. More importantly, $c_{r,m}$ ($m \geqslant 2$) of the harmonic modes are quickly adjusted to follow $c_{r,1}$ in the first few days after their emergence. The relation $c_{r,m} \approx c_{r,1}$ holds after day 20, meaning that these modes propagate northward at approximately the same speed. Consequently, the fundamental and harmonic modes are in a phase-locking state, as also observed by Sutyrin *et al.* [19] in their PE model for the Gulf Stream jets. In fact, such a phase-locking mechanism between the fundamental mode and its temporal or spatial harmonics is quite universal in nonlinearly evolving shear flows [62], which allows a powerful nonlinear interaction to occur within the critical layers where $c_r \approx V_B$.

The results of the $r_R^* = 0.075\,\mathrm{day}^{-1}$ case are shown in Figs. 5(d)–5(f), which share the same qualitative features with the $r_R^* = 0.050\,\mathrm{day}^{-1}$ case. Since the linear growth rate is lower, the perturbation in the $r_R^* = 0.075\,\mathrm{day}^{-1}$ case experiences a longer growth before saturation. Meanwhile, the locked phase velocity retains at a higher value, and the perturbation energy at saturation is lower, suggesting milder distortion to the basic flow.

The energy budget is analyzed to provide insights into the dynamics in Fig. 5. The growth-rate decomposition results for case $r_R^* = 0.075\,\mathrm{day}^{-1}$ are shown in Fig. 6 based on TE. For the

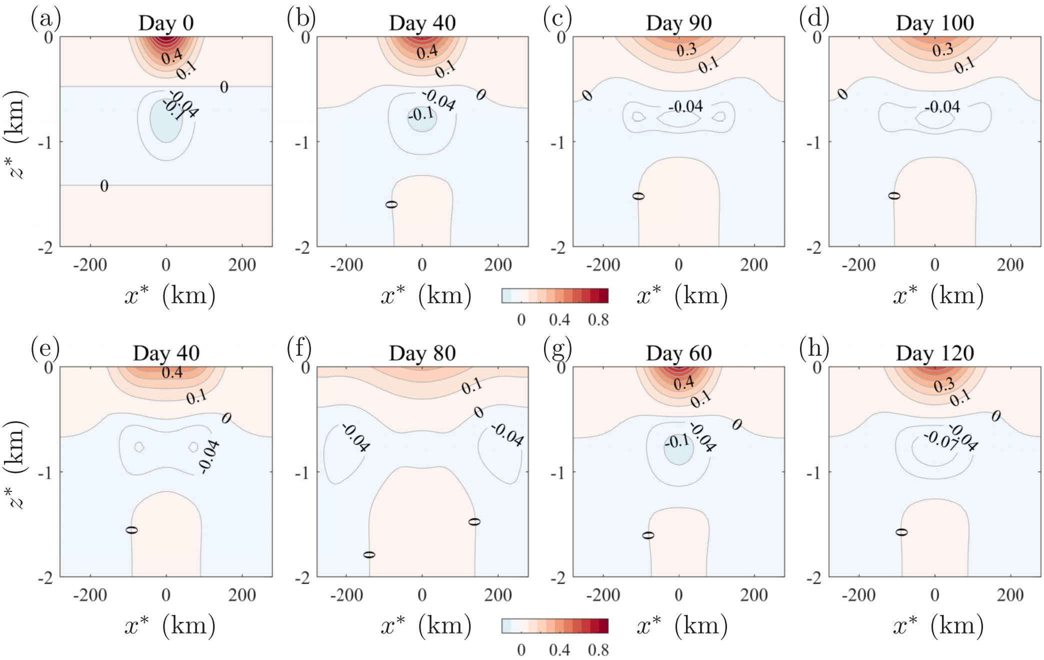

FIG. 7. Temporal sequence of the meridionally averaged meridional velocity (m/s) for the upper-mode [(a)–(d)] $r_R^* = 0.075\,\mathrm{day}^{-1}$ case, [(e), (f)] $0.050\,\mathrm{day}^{-1}$ case, and [(g), (h)] $0.10\,\mathrm{day}^{-1}$ case.

fundamental mode, $\chi_{E,\mathrm{BC}}$ slightly varies and remains the largest throughout, while BT keeps contributing positively. Nevertheless, the total growth rate ω_i is gradually dragged down to zero (reaching saturation) by NL. The nonlinear term is conservative among all scales, so the loss of NL by the fundamental mode converts to the forcing to MFD and other harmonic modes. For the $2k_{y0}$ and $3k_{y0}$ modes, BT is increasingly stabilizing with the rise of k_y before saturation, suggesting barotropic decay due to strong momentum fluxes [13,63]. Meanwhile, BC contributes negligibly or negatively, and both BC and BT tend to diminish, so the saturation of these harmonic modes is primarily a balance between NL and RF. In addition, DP has small negative contributions to the three modes, but it tends to be more pronounced with m increased due to the decreasing scale of motions.

As mentioned in Sec. I, an important question is whether the current and undercurrent can be sustained subject to nonlinear BCI. Therefore, the meridionally mean field and flow structures are studied at different r_R. First, the temporal sequence of the averaged velocity $\bar{V}'$ (defined in Sec. II B) is displayed in Figs. 7(a)–7(d) for the $r_R^* = 0.075\,\mathrm{day}^{-1}$ case. The averaged velocity retains its shape in the first 40 days, but rapidly deforms later on. The upper-layer current gradually decreases in strength and becomes broadened due to the down-gradient eddy fluxes [11,12]. Meanwhile, the undercurrent is weakened and develops into a multipeak pattern aligned zonally. At day 90, for example, three velocity peaks ($\sim -0.05\,\mathrm{m/s}$) are present within a zonal distance of 210 km. This MFD structure is maintained by the balance between NL and RF (note that BC and BT are always zero for MFD because $\hat{u}_0' = \bar{U}' = 0$). As the MFD mode becomes saturated after day 70, $\bar{V}'$ also retains its shape, indicating steady meridional volume flux. The time sequences of $\bar{V}'$ in the other two cases are shown in Figs. 7(e)–7(h). In the case $r_R^* = 0.050\,\mathrm{day}^{-1}$, the upper-layer current is more severely weakened than in the case $r_R^* = 0.075\,\mathrm{day}^{-1}$, but it still remains one core. In comparison, the undercurrent develops into a two-core structure in the saturation regime with the core centers far apart. This signifies a prominent passive response of the undercurrent to the upper-layer instability, as the undercurrent is much weaker in strength than the upper one. On the other hand, the MFD

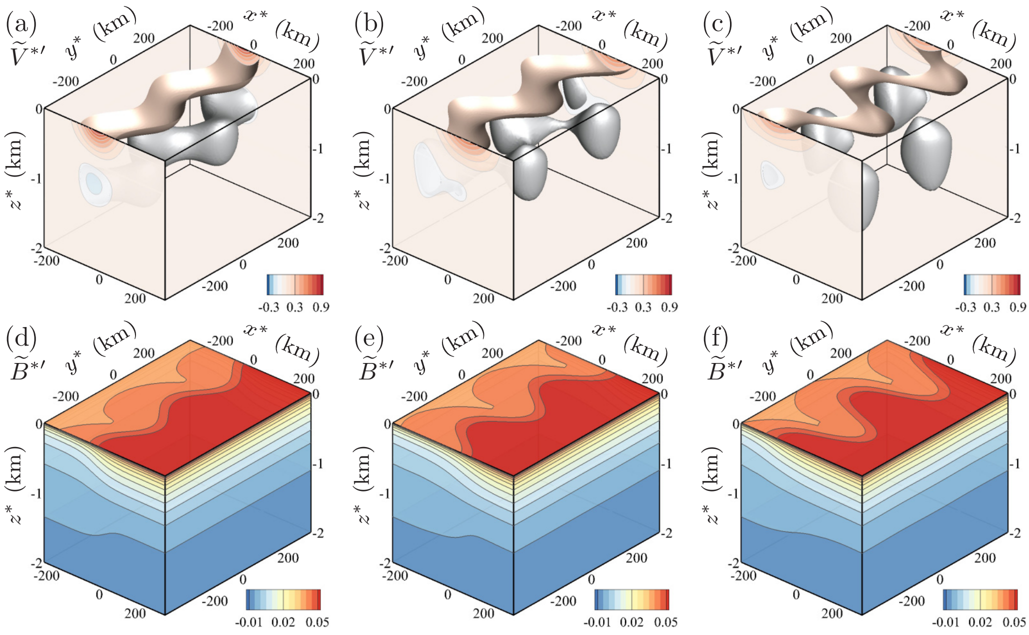

FIG. 8. 3D view of the instantaneous [(a)–(c)] meridional velocity (m/s) and [(d)–(f)] buoyancy (m/s^2) fields in the saturation regime for the upper-mode [(a), (d)] $r_R^* = 0.10$ (day 110), [(b), (e)] 0.075 (day 80), and [(c), (f)] 0.050 day^{-1} (day 60) cases. The isosurfaces in panels [(a)–(c)] are 0.3 m/s (upper) and −0.06 m/s (lower), respectively.

growth in the $r_R^* = 0.10\,\text{day}^{-1}$ case is much milder than the other two cases, because of the low linear growth rate and low perturbation amplitudes in the saturation regime. Consequently, $\bar{V}'$ only slightly differs from the initial field, and the undercurrent remains one core.

The instantaneous velocity and buoyancy fields ($\widetilde{V}'$ and $\widetilde{B}'$) in the saturation regime are depicted in Fig. 8 for the three r_R cases. The meridionally varying perturbations lead to the classic meandering pattern of velocity and buoyancy. The phase-locking state of different Fourier modes suggests that the meander moves northward as a whole. Meanwhile, a clear trend is that as r_R decreases, the flow experiences stronger meanders due to the diminishing restoring force. In the case $r_R^* = 0.050\,\text{day}^{-1}$, the zonal meander scale of the upper-layer current is already comparable to the meridional scale λ_y. Furthermore, the undercurrent is more severely affected by the nonlinear eddy forcing than the upper-layer current, as observed in Fig. 7, so that it is divided into two separate water masses staggered meridionally in Fig. 8(c). Also, the subsurface flow is filled with northward and southward eddies, so the undercurrent is hardly identified. Since the current and undercurrent are largely weakened in the $r_R^* = 0.050\,\text{day}^{-1}$ case, the isopycnals are zonally flattened, especially in the upper layer; instead, the strong tilting of isopycnals shifts to the meridional direction (seen from the surface contours).

The dynamics of the meanders are further studied by analyzing the energy budget. As noted earlier, the meridionally mean field in the saturation regime is maintained primarily by NL and RF, so we first plot the nonlinear term $\hat{\mathbf{F}}_0'$ of the MFD mode in Fig. 9(a). The restoring force $(-r_R\hat{q}_0')$ exhibits a nearly identical distribution except for opposite signs, so $\hat{q}_0'$ is directly reflected. The vertical distribution of $\hat{\mathbf{F}}_0'$ (and $\hat{q}_0'$) well corresponds to $Q_{B,x}$ in Fig. 3(f). The undercurrent and even deeper waters cannot resist the intense eddy momentum fluxes from the strong upper-layer current, so multiple velocity peaks are generated (see also Fig. 8). In addition to the budget of the MFD mode, the instantaneous eddy fluxes $u'q'$ and $v'q'$ at the surface are plotted in Figs. 9(b) and 9(c). Although instantaneous fluxes are generally of less interest for parametrization than the averaged

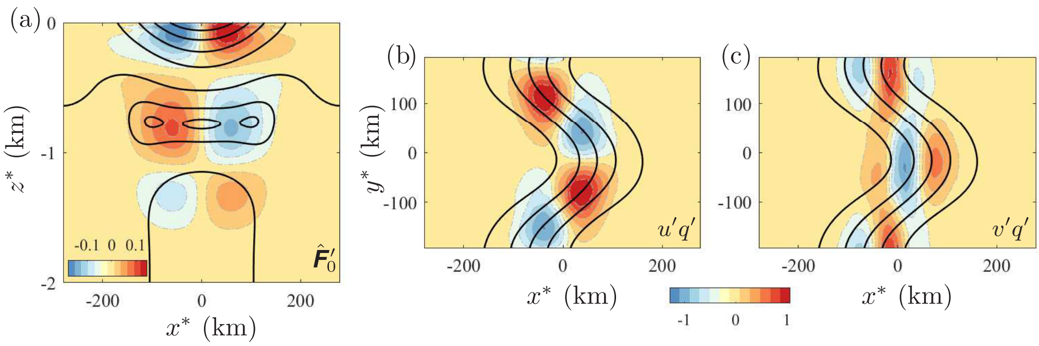

FIG. 9. Vertical section of (a) the nonlinear term $\hat{\mathbf{F}}_0'$ for the MFD mode, and the horizontal sections of the eddy fluxes (b) $u'q'$ and (c) $v'q'$ at the surface in the upper-mode $r_R^* = 0.075\,\text{day}^{-1}$ case (day 80). The black lines in panel (a) denote $\bar{V}'$ as in Fig. 7, and those in panels (b) and (c) denote contours of the stream function.

ones, $u'q'$ and $v'q'$ are focused on because they represent a kind of phase-averaged value relatively static to the meander, which is attributed to the saturation and phase-locking state. The other two commonly used fluxes $u'b'$ and $v'b'$ are not displayed because they look qualitatively similar to the PV counterparts except for opposite signs, which aligns with the parametrization suggestion [64] under a minor BT contribution. The eddy fluxes in Fig. 9 indicate a down-gradient tilting of the meander, which is finally balanced by the prescribed forcing.

B. Lower-mode case

Compared to upper-layer currents, the nonlinear BCI for undercurrents has been rarely studied before. Here, the lower-mode case is investigated, which has important distinctions from the upper-mode cases. For convenience of studying the interaction between the upper and lower modes, the wavenumber of the lower mode is selected to be three times the most unstable upper one, i.e., $k_{y0}^* = 0.048\,\text{km}^{-1}$, which is close to the most unstable lower mode (see Fig. 3). Only one case $r_R^* = 0.010\,\text{day}^{-1}$ is computed due to its relatively low linear growth rate. Similar to Fig. 5, the temporal evolution of the amplitudes and phase velocities of different Fourier modes are shown in Fig. 10. The FNS results are displayed as well to demonstrate the reliability of the nonlinear instability calculation. As in the upper-mode cases, the lower fundamental mode also reaches saturation after a weak linear amplification; the maximum A_1 and A_0 are only $\sim$0.04 and $\sim$0.06. Meanwhile, the fundamental mode and its harmonics are phase locked in the saturation regime, flowing at a common $c_r \approx -0.05\,\text{m/s}$ southward. Nevertheless, nearly all the modes start to decay after day 70, and their phase velocities begin to differ, suggesting a phase-(re)unlocking process.

The temporal sequence of meridionally mean flow is displayed in Fig. 10(c). Interestingly, the upper-layer current is negligibly affected by the nonlinear growth of the lower mode. Figure 11(a) further suggests that the upper-layer current experiences little meanders throughout, which is jointly contributed by two factors. First, the lower mode is active near the undercurrent bottom according to the PV distribution, away from the upper layer (Fig. 3). Second, the undercurrent is much weaker than the upper-layer one. The lower-mode perturbation grows to distort the undercurrent, and even pump deeper water ($>$1400 m) southward at $\bar{V}'^* \approx -0.05\,\text{m/s}$. As shown in Fig. 11, the instantaneous velocity isosurface of the undercurrent is toothlike. Strong meanders are present with the zonal scale comparable to $\lambda_y^* = 130\,\text{km}$. Nevertheless, the undercurrent is not split into multiple cores, and remains in a much narrower region ($\lesssim$200 km), compared with the upper-mode case.

Next, the energy budget of the lower-mode case is investigated. The growth-rate decomposition for different modes based on TE is plotted in Fig. 12. A clear distinction from the upper-mode cases is that the damping effect of DP is prominently enhanced, simply due to the much smaller

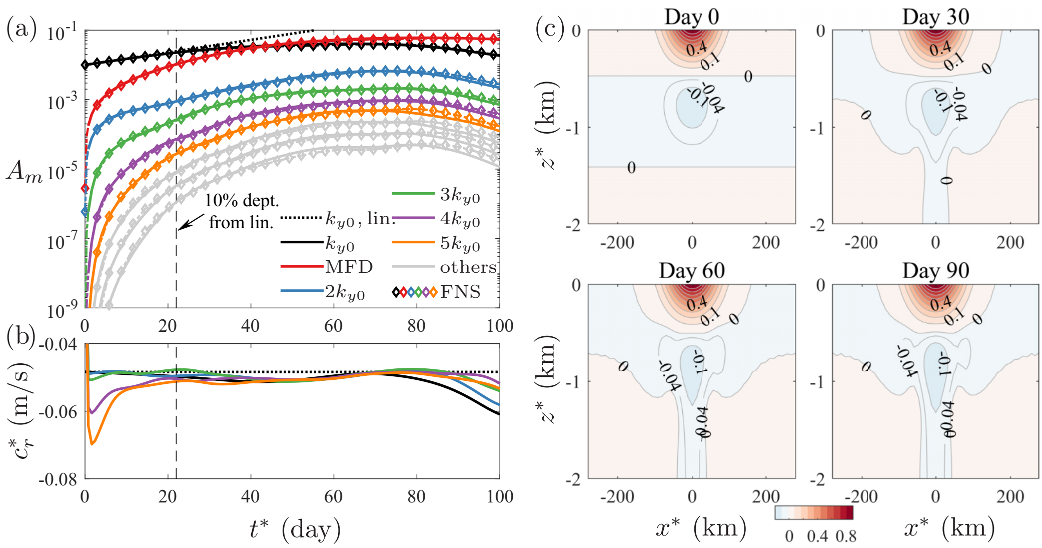

FIG. 10. Lower-mode case: temporal evolution of the (a) amplitudes and (b) phase velocities of different modes, and the (c) temporal sequence of the meridionally averaged meridional velocity ($\bar{V}'^*$, m/s) for the case $r_R^* = 0.010\,\mathrm{day}^{-1}$. The linear results are also shown in panels (a) and (b) for reference.

meridional length scales of the lower mode and its harmonics. For the $k_y = 3k_{y0}$ mode in Fig. 12(c), DP becomes the largest energy sink after day 20, and such damping effects are more severe for higher harmonics ($k_y \geqslant 4k_{y0}$). Consequently, the pronounced viscous effects lead to an overall decay of different modes in the late stage and also the phase unlocking, because DP is highly sensitive to the modal length scales. For the fundamental mode, the BC component, which drives the initial linear growth, continuously decreases and finally falls to negative. Accordingly, the total growth rates of the fundamental and other modes keep dropping, so there are no strict equilibrium regions $\omega_i \approx 0$ as in Fig. 6.

Finally, we highlight that there are indeed some indications of the above nonlinear instability process in model observations. In Fig. 1, the two NEUC jets at $\sim 9\,^\circ$N and $\sim 12\,^\circ$N are distributed on the two sides of the NEC (centered at $\sim 10\,^\circ$N), resembling the patterns in Fig. 7(f). Also, the

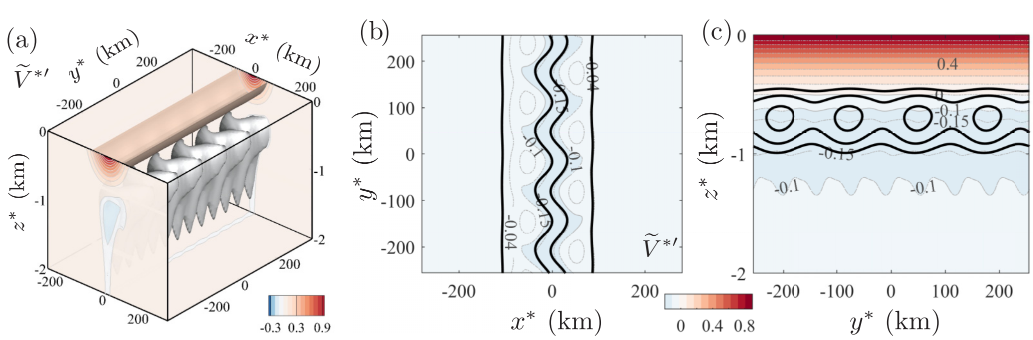

FIG. 11. (a) 3D visualization of the instantaneous meridional velocity ($\tilde{V}'^*$, m/s) in the saturation regime (day 60) for the lower-mode $r_R^* = 0.010\,\mathrm{day}^{-1}$ case. (b) The horizontal section at depth 780 m and (c) the y-z section at $x = 0$. The black lines denote contours of the stream function.

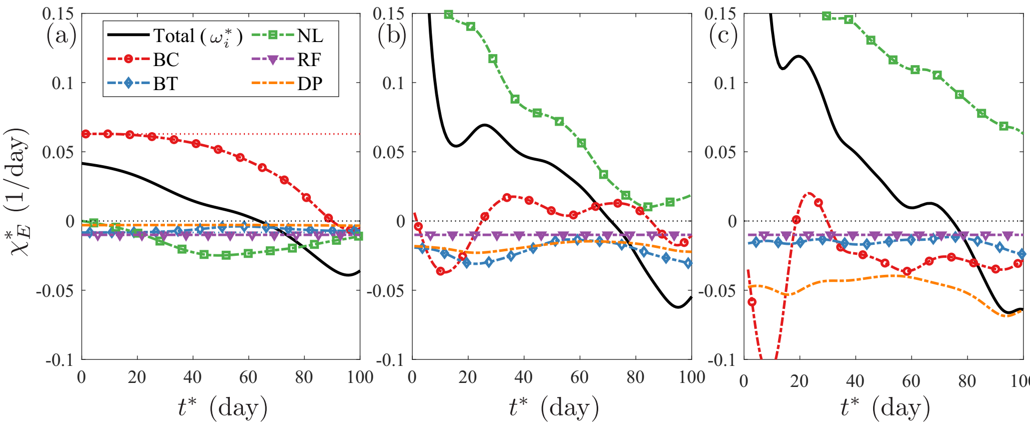

FIG. 12. Growth-rate decomposition based on TE for the (a) fundamental, (b) $k_y = 2k_{y0}$, and (c) $k_y = 3k_{y0}$ modes in the lower-mode $r_R^* = 0.010\,\text{day}^{-1}$ case. The dotted lines in panel (a) are the linear reference. The term notations are the same as in Fig. 6.

three NEUC jets all extend deeply over 2000 m depth, reminiscent of the phenomenon in Fig. 10(c). Further clarification on this point is still anticipated in future work.

C. Model with minimal modes

It is observed in Secs. IV A and IV B that the amplitudes of the high-k_y harmonic modes are orders of magnitude smaller than the fundamental and MFD modes, so it is interesting to explore a model of minimal modes that is adequate to describe the nonlinear saturation process. Such a simple model can also maximize the advantage of the developed nonlinear instability framework.

The simplest choice is a three-mode model ($M = 2$), comprised of the fundamental, MFD, and the lowest harmonic $k_y = 2k_{y0}$ modes. For reference, the computation in the previous sections with $M = 10$ is termed the full model. The temporal evolution of different modes is examined in Fig. 13 for representative upper- and lower-mode cases, respectively. Even with only three modes, this reduced model can well predict the nonlinear growth and saturation amplitude of the fundamental and MFD modes. However, the harmonic mode and the c_r of the fundamental mode cannot be well resolved, which strongly oscillate around or above the full-model values. This is ascribed to the imbalance of the nonlinear term, where the interaction of higher harmonics is truncated and thus cannot be "received" by the three activated modes. Observing the rapid decrease of A_m with m, we additionally include the $k_y = 3k_{y0}$ mode, which constructs a four-mode model. As shown in Fig. 13, the oscillations of c_r and A_2 are clearly suppressed in both the upper- and lower-mode cases, so they are quite close to the full model results. Nevertheless, c_r in the four-mode model tends to be overpredicted near the end of the saturation, due to the slow decay of the fundamental and MFD modes.

In short, the nonlinear growth and saturation of the present current-undercurrent system is governed by the leading (in terms of k_y) few modes. Using only a three-mode model can well predict the saturation amplitude of the perturbation, while adding the fourth mode can largely improve the prediction of phase velocity and higher harmonics.

V. SECONDARY INSTABILITY RESULTS

Although Sec. IV indicates that the baroclinic unstable modes result in nonlinear saturation of the current and undercurrent, it is important to study the instability of the saturation state, i.e., its secondary instability, to answer whether the saturation can be sustained. Moreover, we intend to

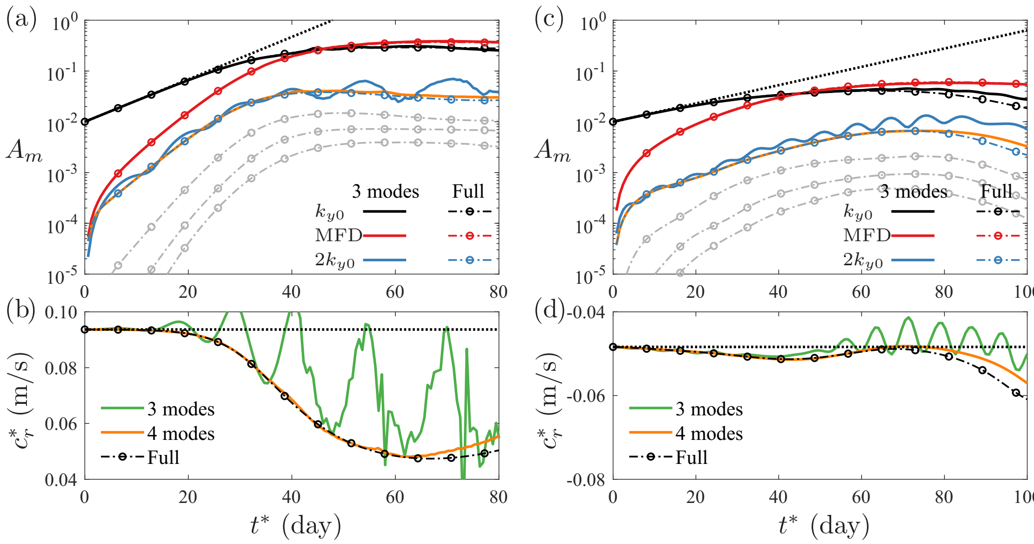

FIG. 13. Temporal evolution of the [(a), (c)] amplitudes of different modes and [(b), (d)] phase velocity of the fundamental mode using the full, three-mode, and four-mode models, for the [(a), (b)] upper-mode ($r_R^* = 0.050\,\mathrm{day}^{-1}$) and [(c), (d)] lower-mode ($0.010\,\mathrm{day}^{-1}$) cases.

reveal the prominent role of detuned resonance for undercurrents, which received little attention before.

A. Upper-mode case

The $r_R^* = 0.050\,\mathrm{day}^{-1}$ case is studied first, which experiences the strongest meanders. The saturation state at day 60 is focused on. Due to the high cost of SIA, it is important to determine the number of terms truncated, M_s or N_y, in the Floquet series in Eq. (14). We use three convergence criteria to determine M_s: (i) the subharmonic case gives identical results (relative error of σ_s less than 1%) as the $\varepsilon_d = 0.5$ detuned case; (ii) the detuned case gives identical results when ε_d is varied by an integer (the same criterion for σ_s; ε_d ranged from -1 to 1); and (iii) the energy portion of the highest $|m + \varepsilon_d|$ mode to $\hat{E}_s''$ is less than 0.1% (see Table II for details). In general, $M_s = 5$ ($N_y = 10$ or 11) is adequate for the present calculations.

Figure 14 presents an overview of the SIA results as a function of ε_d, where several unstable modes are identified. Since σ_s is a continuous function of ε_d, we classify these modes according to the location of their peak growth rates. The most unstable mode peaking at $\varepsilon_d = 0$ reflects the fundamental resonance, so it is termed the F_1 mode. Meanwhile, this mode has a comparable frequency with the basic flow ($\sigma_{s,i} \approx 0$) when highly unstable ($|\varepsilon_d| < 0.25$). There are three

TABLE II. Energy portion of each wavenumber component for the most amplified fundamental (F_1), subharmonic (S_1) and detuned (F_1, $\varepsilon_d = 0.24$) secondary modes, for the upper-mode $r_R^* = 0.050\,\mathrm{day}^{-1}$ case.

Fundamental	Wavenumber $(m + \varepsilon_d)$	−4.00	−3.00	−2.00	−1.00	0.00	1.00	2.00	3.00	4.00
	Energy portion (%)	0.4	1.1	3.2	31.8	26.6	31.8	3.2	1.1	0.4
Subharmonic	Wavenumber $(m + \varepsilon_d)$	−3.50	−2.50	−1.50	−0.50	0.50	1.50	2.50	3.50	
	Energy portion (%)	0.6	2.1	24.7	9.1	53.2	7.7	1.9	0.8	
Detuned	Wavenumber $(m + \varepsilon_d)$	−3.76	−2.76	−1.76	−0.76	0.24	1.24	2.24	3.24	4.24
	Energy portion (%)	0.6	1.8	6.1	18.3	38.7	31.2	2.2	0.8	0.4

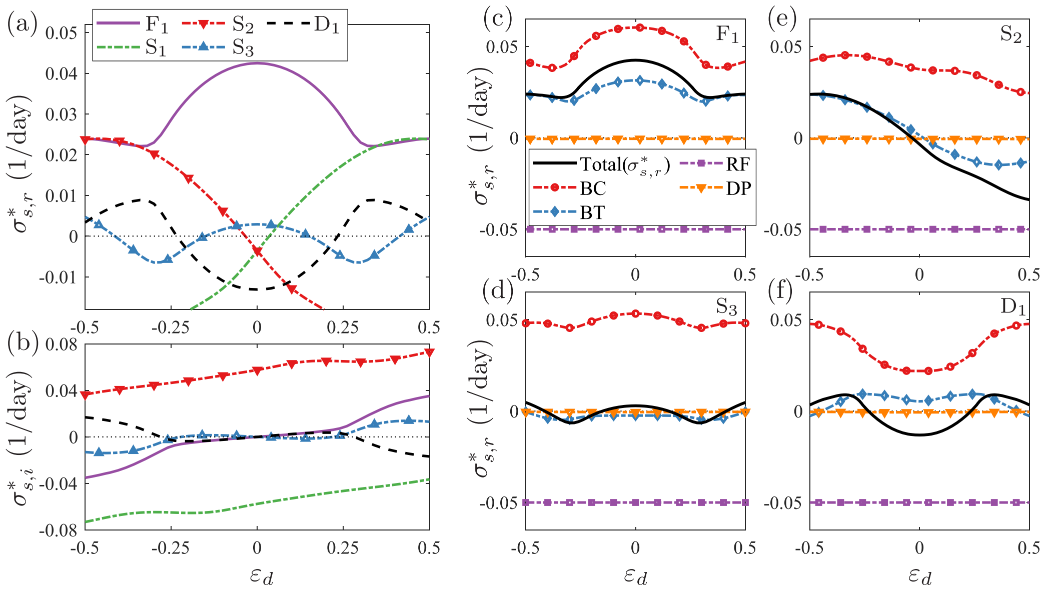

FIG. 14. (a) Growth rates and (b) frequency shifts of different secondary instability modes as a function of the Floquet detuning parameter for the upper-mode $r_R^* = 0.050\,\mathrm{day}^{-1}$ case. [(c)–(f)] Growth-rate decomposition based on TE for the F_1, S_2, S_3, and D_1 modes; F, S, and D represent fundamental, subharmonic, and detuned modes, respectively. The term notations are the same as in Fig. 6.

unstable modes most amplified at $\varepsilon_d = 0.5$ or -0.5, so they are termed the S_1–S_3 modes ("S" for subharmonic). Besides, a D_1 mode reflecting the detuned resonance exists, which is most unstable at $\varepsilon_d = 0.32$. The growth rates of these modes are lower than the primary instability, so rapid breakdown of the saturated meanders is not anticipated. This essentially differs from, e.g., the inertia-dominated bottom boundary layer case [53], where $\sigma_{s,r}$ can be an order of magnitude higher than the primary instability. This modest secondary instability also explains why the FNSs in Fig. 5 stay saturated without breakdown, though exposed to various random fluctuations. The growth-rate decompositions of these modes are shown in Fig. 14, where BC contributes the most energy to all modes throughout ε_d. Also, BT has pronounced contributions to modes F_1, S_1, and S_2, so they can be regarded as a mixed BC-BT type. This mechanism of joint BC and BT contributions to secondary instability also exists in the atmospheric cyclogenesis in localized baroclinic zones [65]. Besides, DP has minor effects throughout, as for the primary instability (upper-mode case).

Next, the structures of these secondary instability modes are discussed. Table II lists the energy ratios of the leading Floquet waves to the total perturbation energy $\hat{E}_s''$ for the three modes of high growth rates. Over 90% of $\hat{E}_s''$ resides in the leading three Floquet waves, because of the rapid decrease of A_m with m in the primary instability. These secondary instability modes are most amplified near the surface, so the $\hat{\psi}_s''$ contours of these three modes are depicted in Fig. 15 at the surface and around the undercurrent core, which are normalized as $\hat{E}_s'' = 1$. The F_1 mode has the same meridional wavenumber as the basic flow. The perturbation takes the form of cyclones ($\hat{\psi}_s''$ peaks) and anticyclones (valleys) around the meander, as previously reported in numerical and observational works [19,57,65]. These cyclones and anticyclones have comparable zonal and meridional sizes of ~200 km, and appear where the current has strong cross-stream motions. They move northward at the same phase speed as the basic flow since $\sigma_{s,i} \approx 0$, and can reach down to the subsurface region to further distort the undercurrent. In comparison, for the S_1 mode, the k_y of the leading Floquet wave is two times the meander, and the surface cyclones are oblique and compressed. For more insights into the structures of these modes, the horizontal and vertical shear of the secondary basic flow are depicted in Figs. 15(e) and 15(f), whose expressions are indicated by

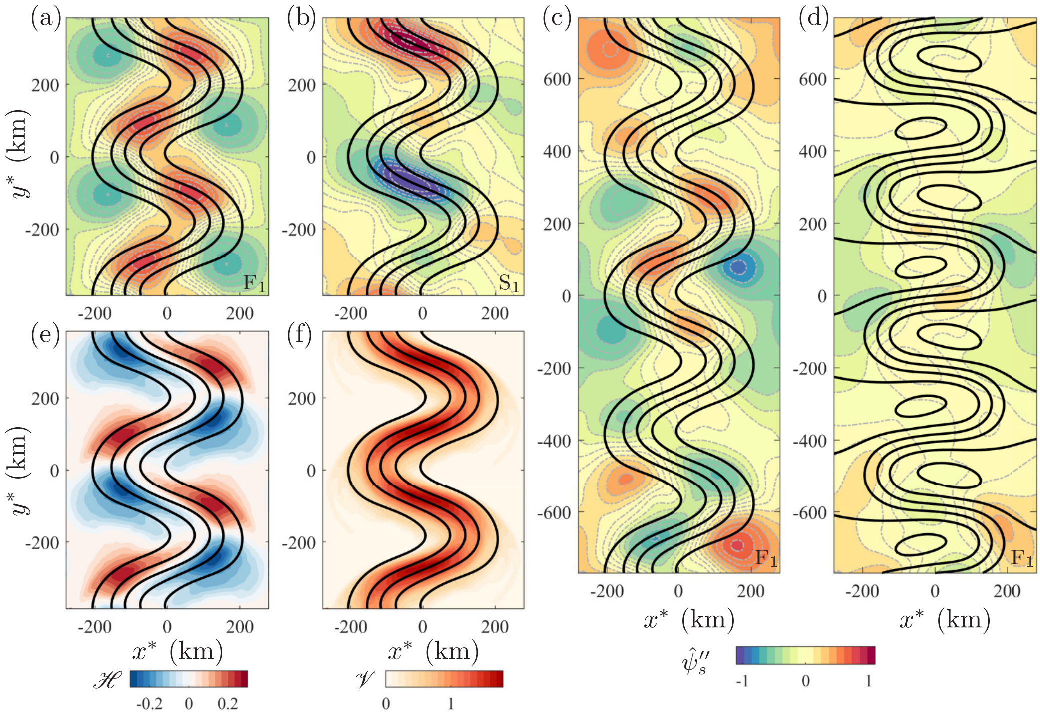

FIG. 15. Horizontal sections of the secondary perturbation stream function ($\hat{\psi}_s''$) for the most amplified (a) fundamental (F_1), (b) subharmonic (S_1) and [(c), (d)] detuned modes (F_1, $\varepsilon_d = 0.24$), for the upper-mode $r_R^* = 0.050\,\mathrm{day}^{-1}$ case. Panels (a)–(c) are at the surface and panel (d) is at depth 780 m. The last two panels are the (e) horizontal shear ($\mathscr{H} = (\partial \tilde{u}'^*/\partial x^* - \partial \tilde{v}'^*/\partial y^*)/f_0^*$) and (f) vertical shear ($\mathscr{V} = [(\partial \tilde{u}'^*/\partial z^*)^2 + (\partial \tilde{v}'^*/\partial z^*)^2]^{1/2}/N_0^*$) of the basic flow at the surface. The black dotted lines are the contours of the basic-flow stream function.

budget equation (19). Since the F_1 and S_1 modes are BC dominated, the locations of the cyclones and anticyclones well correspond to those of strong vertical shear. Also, the regions of intense horizontal shear are surrounded by enriched perturbations, reflecting the notable contribution of BT. The above connection between cyclonic perturbations and the horizontal and vertical shear of the mean flow can be utilized to identify secondary instability in observational and simulation results. Finally, the detuned case is displayed in Figs. 15(c) and 15(d). Cyclones and anticyclones can still be observed, but they are out of phase with the basic flow due to their detuned frequencies and wavenumbers. Consequently, the meander can quickly become meridionally aperiodic. Therefore, the SIA not only reveals the forms of the perturbation that meanders are most susceptible to, but also reflects the mechanism of how wideband aperiodic cyclones are induced.

For the cases $r_R^* = 0.075$ and $0.10\,\mathrm{day}^{-1}$, the secondary instability is much weaker, due to the weaker meanders and stronger restoring force. Consequently, no unstable modes are found in the latter case ($0.10\,\mathrm{day}^{-1}$); only a weak F_1 mode is identified in the former case, which shares a lot of common features with that in Fig. 15, but the maximum growth rate is only $0.005\,\mathrm{day}^{-1}$. Therefore, the secondary instability results for these two cases are not further discussed.

B. Lower-mode case

The secondary instability of undercurrents has been rarely investigated before, so we proceed to study the lower-mode $r_R^* = 0.010\,\mathrm{day}^{-1}$ case. As discussed in Sec. IV B, the meander experiences a

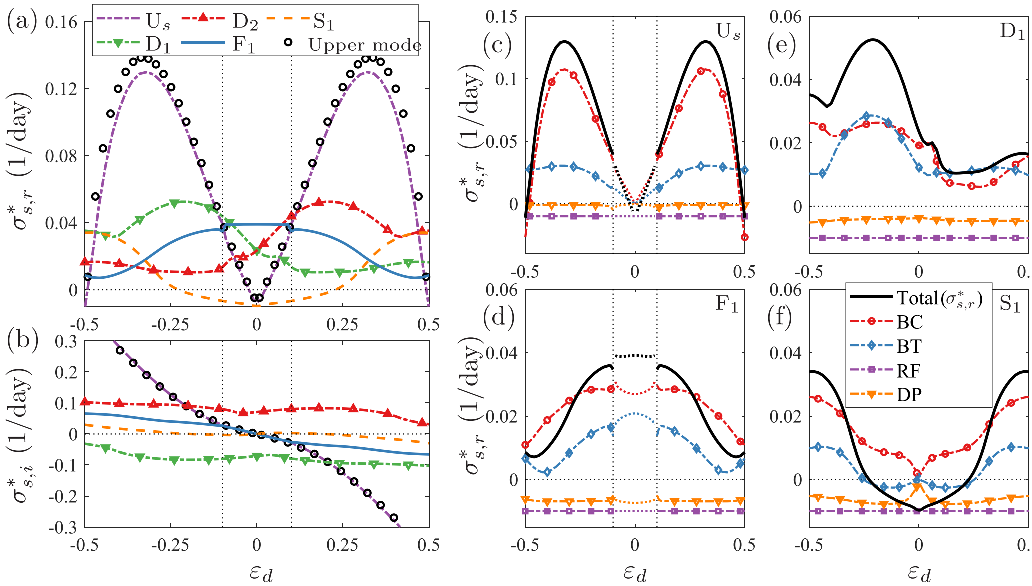

FIG. 16. (a) Growth rates and (b) frequency shifts of different secondary instability modes as a function of the Floquet detuning parameter for the lower-mode $r_R^* = 0.010\,\mathrm{day}^{-1}$ case. [(c)–(f)] Growth-rate decomposition based on TE for the U_s, F_1, D_1, and S_1 modes, respectively. The results in the synchronization region (see text) between U_s and F_1 are plotted in dotted lines.

decay after reaching saturation, so we select day 65 for SIA, when the fundamental mode reaches its maximum amplitude ($\omega_{i,1} \approx 0$). In later stages when the saturation decays, the secondary instability modes may not dominate because of their lower growth-rate amplitude than the primary instability.

As in Sec. V A, a series of unstable modes are identified in Fig. 16. A significant distinction is that there appears a detunedlike mode whose maximum growth rate is over two times the lower mode in the primary instability. In fact, we confirm that this mode is the counterpart of the upper mode in the primary instability, thus termed the U_s mode, simply because the upper-layer current remains nearly unaltered by the nonlinear evolution of the lower mode (recall Fig. 11). As a result, the upper-layer current still succumbs to the upper-mode primary instability. For a more quantitative comparison, we replot the upper-mode results from Fig. 3 using the conversion relation

$$k_{y,\text{upper}} \leftrightarrow \pm\varepsilon_d k_{y,\text{lower}},$$
$$-\mathrm{i}(\pm\omega_{r,\text{upper}} + \mathrm{i}\omega_{i,\text{upper}}) \leftrightarrow \pm\mathrm{i}(\sigma_{s,i} - \varepsilon_d\omega_{r,\text{lower}}) + \sigma_{s,r}, \tag{21}$$

deduced from Eq. (14), where $\pm$ represents conjugate modes. The frequencies of U_s and the upper mode match well with each other, but the U_s mode has a lower growth rate. This is reasonable because the basic undercurrent in the U_s case has reached saturation, which consumes part of the energy and thus is stabilizing. Thereby, the U_s mode results reflect an interaction between the upper and lower modes. Figure 16(c) gives the growth-rate decomposition of the U_s mode, which closely resembles the upper mode results in Fig. 3(c). Table III and Fig. 17 provide the energy distribution among Floquet waves and the perturbation structure for the most unstable U_s mode. Over 96% of the energy resides in the leading $m + \varepsilon_d = 0.32$ waves, which is surface amplified and meridionally aligned as the upper mode. Down to the undercurrent region, small-amplitude tilted cyclones and anticyclones are present around the narrow undercurrent meander.

The other modes in Fig. 16 besides U_s are subsurface amplified, so they result directly from the secondary instability of the undercurrent meanders. According to the ε_d location of their maximum growth rate, these modes are termed the D_1, D_2, F_1, and S_1 modes, respectively. A notable point is

TABLE III. Energy portion of each wavenumber component for the most amplified detuned (U_s, $\varepsilon_d = 0.32$), detuned (D_2, $\varepsilon_d = 0.22$), and subharmonic (S_1) secondary modes, in the lower-mode $r_R^* = 0.010\,\mathrm{day}^{-1}$ case.

Detuned (U_s)	Wavenumber ($m + \varepsilon_d$)	−3.68	−2.68	−1.68	−0.68	0.32	1.32	2.32	3.32	4.32
	Energy portion (%)	0.0	0.0	0.2	2.6	96.1	0.7	0.1	0.0	0.0
Detuned (D_2)	Wavenumber ($m + \varepsilon_d$)	−3.78	−2.78	−1.78	−0.78	0.22	1.22	2.22	3.22	4.22
	Energy portion (%)	0.2	0.6	2.1	43.8	27.4	23.8	1.4	0.6	0.1
Subharmonic	Wavenumber ($m + \varepsilon_d$)	−3.50	−2.50	−1.50	−0.50	0.50	1.50	2.50	3.50	
	Energy portion (%)	0.3	1.4	11.7	32.6	50.1	2.5	1.1	0.2	

that the detuned resonance dominates the secondary instability of undercurrents. From the energy budget, the DP term is evidently stabilizing for the above four modes, as in the primary instability. The S_1 mode is classified as a baroclinic mode, while the D_1, D_2, and F_1 modes are more like a BT-BC mixed type. Therefore, the significant role of the BT component for the restricted undercurrent meanders contributes to the dominant detuned resonance. Since they are subsurface amplified, only the perturbation structures around the undercurrent region are shown in Figs. 17(b) and 17(c) for the most unstable D_1 and S_1 modes. The secondary cyclones and anticyclones are confined in the narrow region of the undercurrent meanders, exhibiting strong aperiodicity in terms of the basic flow. The scales of these cyclones are down to below 100 km, so more enhanced ageostrophy is anticipated subsequent to the secondary instability process. Moreover, the connection between cyclonic perturbations and the horizontal and vertical shear of the basic flow is also observed.

Another notable point is the seeming discontinuity in the growth rate for modes U_s and F_1 near $\varepsilon_d = \pm 0.1$, which is more clearly seen in Figs. 16(c) and 16(d). This is reminiscent of the mode synchronization phenomenon in the instability theory [66], which occurs when the phase speeds of two modes coalesce [Fig. 16(b)], and can result in branching of the discrete spectrum (discontinuous growth rate due to possibly mode switch). The synchronization also exists, though less obviously, between other modes in Figs. 14 and 16, leading to several turnings of the growth rate curves.

Finally, Fig. 18 provides a 3D view of the most unstable secondary instability modes in the upper- and lower-mode (besides U_s) cases. Although the upper-mode primary instability largely reshapes the undercurrent, the F_1 mode is highly constrained near the surface and does not penetrate deeply downward. Besides, the centers of these cyclones and anticyclones are observed to vary slightly

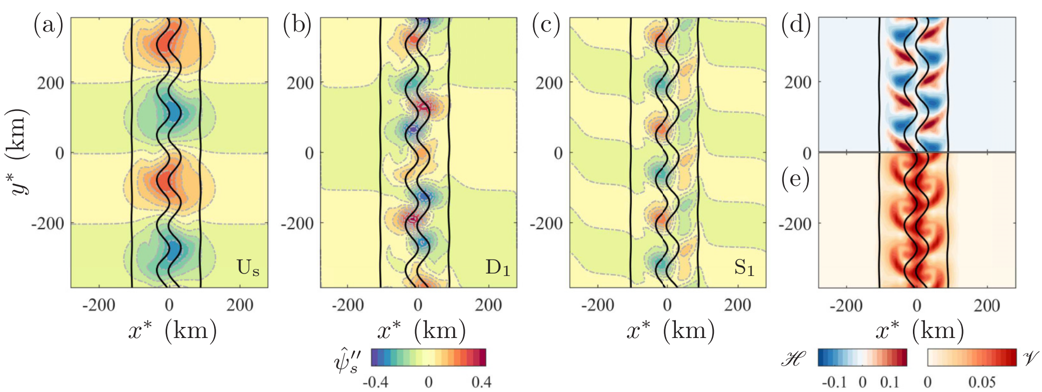

FIG. 17. Horizontal sections of the secondary perturbation stream function ($\hat{\psi}_s''$) for the most amplified (a) detuned U_s ($\varepsilon_d = 0.32$), (b) detuned D_1 ($\varepsilon_d = 0.22$), and (c) subharmonic (S_1) modes, in the lower-mode $r_R^* = 0.010\,\mathrm{day}^{-1}$ case (depth 780 m). The last two panels are the (d) horizontal shear $\mathscr{H}$ and (e) vertical shear $\mathscr{V}$ of the basic flow. The black dotted lines are the stream function contours from the primary instability.

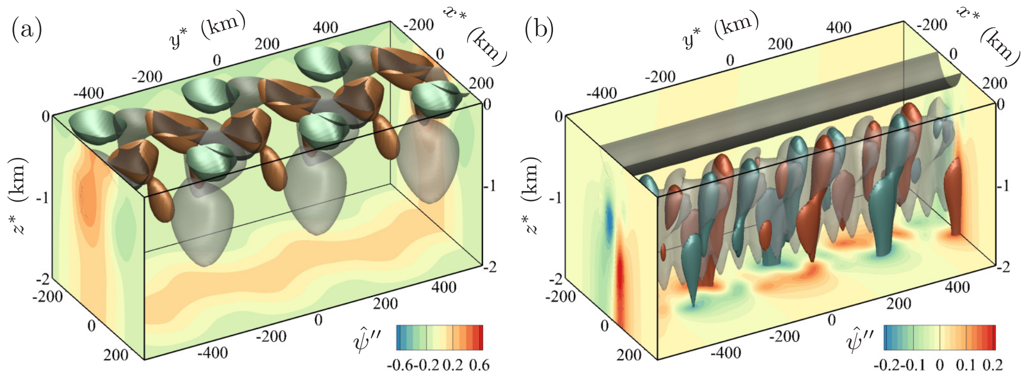

FIG. 18. Isosurfaces of the secondary perturbation stream function for the most amplified modes in the (a) upper mode (fundamental F_1, $\hat{\psi}'' = \pm 0.35$) and (b) lower mode (detuned D_1 at $\varepsilon_d = 0.22$, $\hat{\psi}'' = \pm 0.15$) cases. The black shades are the meridional velocity isosurfaces from the primary instability. The horizontal sections can be found in Figs. 15 and 17.

with depth. In the lower-mode case, the D_1 mode is confined in the undercurrent region, and moves southward with the meander. They are away from the upper-layer current and can drive deeper-layer waters rotating. Nevertheless, the unperturbed upper-layer current is subject to the surface-amplified U_s mode.

VI. SUMMARY

In this work, the nonlinear formation and secondary instability of jet meanders due to BCI is investigated. An idealized current-undercurrent model is extracted from the WPO undercurrent system to study the role of intrinsic instability. We adopt a continuously stratified QG model and start from a smooth basic flow. Two-dimensional eigenmode analysis identifies two primary unstable modes of the baroclinic Charney and Phillips types, respectively, in accordance with the current and undercurrent setup. Comparison of the TGA results with the PE model shows that IGWs rapidly decay in the first two days, so the subsequent linear perturbation growth is dominated by baroclinic eigenmodes.

The most unstable upper and lower modes are initiated to study their temporal evolution. A weakly nonlinear instability framework is developed to resolve the evolution of the initiated fundamental mode, its smaller-scale harmonics, and the MFD. After the initial rapid amplification, these modes reach amplitude saturation and phase locking due to nonlinear interaction. The saturation of the upper mode weakens the current, results in upper-current meanders, and splits the undercurrent into multiple cores. This signifies a prominent passive response of the undercurrent to the upper-layer instability. On the other hand, the saturation of the lower mode leads to undercurrent meanders, which drive deeper waters southward but negligibly affect the upper layer. Observing that the amplitudes of the harmonic modes quickly decrease with the rise of k_y, a model with minimal modes is constructed. The maximum Ro_ζ and minimum Ri do not vary much during the meander formation process, so the flow remains primarily geostrophic, which is in line with previous findings that the QG model can capture the major dynamic events for baroclinic meander problems [18]. Nevertheless, inertial motions tend to be more pronounced due to the relatively strong horizontal shears and small-scale motions [67], which requires more explorations in future work.

Finally, we develop a Floquet-based SIA framework for the saturated meanders, which is a full 3D instability (triglobal) calculation scarcely explored before. The saturation state is found to succumb to modest secondary instability. The fundamental resonance dominates the upper-mode case

(F_1 mode), and the perturbation takes the form of mesoscale cyclones and anticyclones distributed around the meander. Conversely, dominant detuned resonance is observed for the lower-mode case (D_1 mode), which quickly induces aperiodic small-scale motions in terms of the meander. Besides, a unique detunedlike mode with a high growth rate is reported, which is identified as the counterpart of the upper mode in the primary instability.

From the methodological perspective, this work presents a combined nonlinear and secondary instability framework for continuously stratified BCI systems. From the physical perspective, this work highlights a robust mechanism of the formation of baroclinic meanders and mesoscale cyclones and anticyclones due to nonlinear and secondary instabilities, which can be applicable to other current-undercurrent systems in global oceans (introduced in Sec. I). Furthermore, the unique interaction between the current and undercurrent meanders is revealed, which can help understand the formation and sustainability of undercurrents from the instability point of view. For more realistic oceanic flows, we note that the interlayer interaction and the connection between cyclonic perturbations and mean shear revealed in this work can help to identify nonlinear and secondary instabilities in observational and model results, as discussed in Secs. IV B and V A. Besides, the present fully 3D SIA enables an instability analysis on realistic 3D flows extracted from observations or simulations, if the flow unit exhibits quasiequilibrium and quasiperiodicity in one direction.

Future work will focus on extending the limitations of the present model, including consideration of the β effect, ageostrophy and realistic boundaries, and more realistic representation of the restoring forcing.

ACKNOWLEDGMENTS

This research was supported by the NSFC Key Research Project No. 41930539, CORE, a joint research center between Laoshan Laboratory and Hong Kong University of Science and Technology, the Area of Excellence Scheme (AoE/P-601/23-N), and the Hong Kong Research Grants Council (GRF 16212720).

APPENDIX A: ALGORITHMS OF NONLINEAR INSTABILITY ANALYSIS

The inner and outer iterations required in Sec. II B are detailed. The condition of slowly varying $|\hat{\Psi}'_m|$ enables a closure of ω_m, which leads to a local iteration for ω_m at every time step as

$$\omega_m^{(k+1)} = \omega_m^{(k)} + \mathrm{i}\frac{1}{\hat{E}'_m}\iint_\Omega \left(\hat{u}'^{\dagger}_m \frac{\partial \hat{u}'_m}{\partial t} + \hat{v}'^{\dagger}_m \frac{\partial \hat{v}'_m}{\partial t} + \frac{f_0}{\bar{N}^2 \mathrm{Bu}} \hat{b}'^{\dagger}_m \frac{\partial \hat{b}'_m}{\partial t}\right) \mathrm{d}x\mathrm{d}z, \tag{A1}$$

where k is an inner iteration index. Convergence is achieved when $\Delta\omega = |\omega_m^{(k+1)} - \omega_m^{(k)}| < \delta\omega$, where the prescribed criterion $\delta\omega$ is set to 10^{-6} throughout. Equations (9) and (A1) constitute a closed nonlinear system for the unknowns $(\hat{\Psi}'_m, \omega_m)$, where $m = -M, \ldots, M$. In the present model, we use $M = 10$ throughout. Equation (9) is marched implicitly in time to enhance robustness and allow a larger time step. To be specific, $\hat{\boldsymbol{\Psi}}'^{[t_n]}_m$ at the nth time step t_n is solved from

$$\frac{\hat{\boldsymbol{\Psi}}'^{[t_n]}_m - \hat{\boldsymbol{\Psi}}'^{[t_{n-1}]}_m}{\Delta t} = \left(\mathbf{L}_m + \mathrm{i}\omega_m^{[t_n]}\mathbf{I}\right)\hat{\boldsymbol{\Psi}}'^{[t_n]}_m + \frac{\hat{\mathbf{N}}'^{[t_n]}_m}{\mathcal{A}_m^{[t_n]}}, \tag{A2}$$

where the step $\Delta t = t_n - t_{n-1}$, and $[\cdot]$ denotes the outer iteration. Since $\hat{\mathbf{N}}'_m$ is a nonlinear function of $\hat{\boldsymbol{\Psi}}'_m$, a local iteration is required.

The above procedures are summarized as follows. First at $t = 0$, we initialize one or several modes at prescribed amplitudes, and their $(\hat{\Psi}'_m, \omega_m)$ are from the eigenmode analysis. The subsequent procedures at $[t_n]$ are as follows:

(i) Set the initial value $(\hat{\Psi}'^{(0)}_m, \omega_m^{(0)})$ at t_n using that at t_{n-1}, and then obtain $\hat{\mathbf{N}}'^{(1)}_m$.

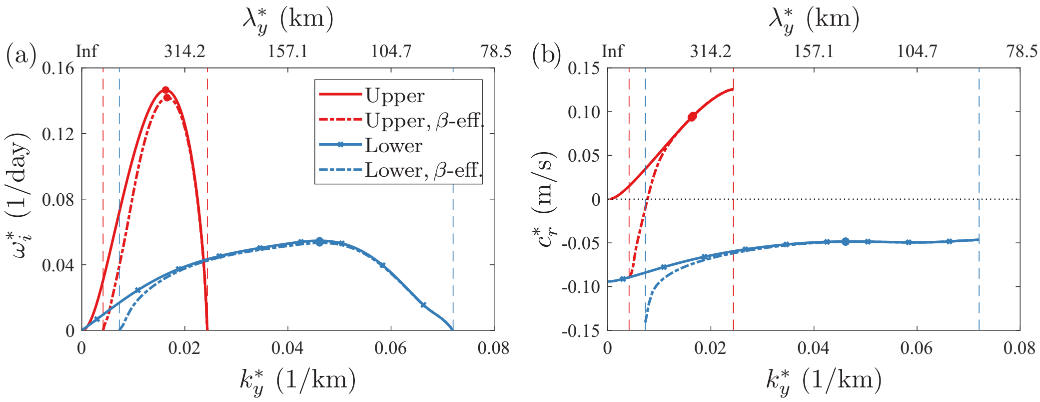

FIG. 19. Linear eigenmode results: (a) growth rates and (b) phase velocities of the upper and lower modes with and without the β effect (eff.).

(ii) Obtain ($\hat{\Psi}_m'^{(p)}$, $\omega_m^{(p)}$) subject to $\hat{\mathbf{N}}_m'^{(p)}$ by iteratively solving Eqs. (A1) and (A2), until $\Delta\omega < \delta\omega$.

(iii) Compute $\hat{\mathbf{N}}_m'^{(p+1)}$ using $\hat{\Psi}_m'^{(p)}$ and $\omega_m^{(p)}$. Repeat steps (ii) and (iii) until each mode converges, under the criterion $\Delta q = \max_m(|\hat{\Psi}_m'^{(p)} - \hat{\Psi}_m'^{(p-1)}|/|\hat{\Psi}_m'^{(p)}|) < \delta q = 10^{-3}$.

(iv) Judge and initiate new nonlinearly excited modes based on $|\hat{\mathbf{N}}_m'|$. Then move to the next time step $[t_{n+1}]$.

APPENDIX B: β EFFECT AND THE SIA SOLVER VERIFICATION

First, the β effect on the linear eigenmode results is evaluated. The nondimensional parameter from Table I is $\beta = \beta^* L^{*2}/U_0^* = 0.269$. For the meridional flow considered, the β effect is not compatible with the zonally periodic boundary condition, so the impenetrable channel wall boundary ($\hat{u}' = 0$ at $x_{\min}$ and $x_{\max}$) is used instead, which negligibly affects the QG eigenmodes in Fig. 3 since the perturbation is concentrated around the jet center. The eigenmode results with and without the β effect (both subject to wall boundary) are compared in Fig. 19. The β effect primarily affects the long-wave region, known to result in the long-wave cutoff and phase velocity decrease [7]. Here, the cutoff for the upper mode occurs at a longer wave than the lower mode, which is anticipated from the Kuo scale $k_{y,\beta}^* \approx \sqrt{\beta^*/|V_B^*|}$ due to its higher speed. In terms of the most unstable modes we concern, the β effect only decreases the maximum growth rates by 3% and 2% for the upper and lower modes, respectively. Also, the corresponding wavenumbers and phase velocities are varied by less than 2%. Therefore, we can conclude that the β effect has a minor effect on the most unstable upper and lower eigenmodes, and also their harmonics at higher k_y. Nonetheless, the β effect, though small, can invalidate the zonally periodic boundary condition and destroy the symmetric and/or antisymmetric pattern of the results, which deserves further discussions in future work.

The Floquet-based SIA solver is verified through a QG Eady-like secondary instability case investigated by Stevens and Hakim [57]. The specific basic flow is an atmospheric Eady jet (Bu = 1) superimposed with a periodic neutral wave (amplitude 1) without harmonics and MFD. In their $\mu = 0$ case (μ is a mean flow parameter defined in the reference), the two most unstable (fundamental-type) Floquet modes at $k_y = 2.5$ have the growth rates $\sigma_{s,r} = 0.35$ and 0.22, and our reproduced results are 0.3556 and 0.2089 using $M_s = 5$. Furthermore, we compare in Fig. 20 the horizontal and vertical sections of the perturbation temperature (counterpart of buoyancy in our oceanic case) of the first Floquet mode. The good agreement demonstrates the reliability of our SIA solver.

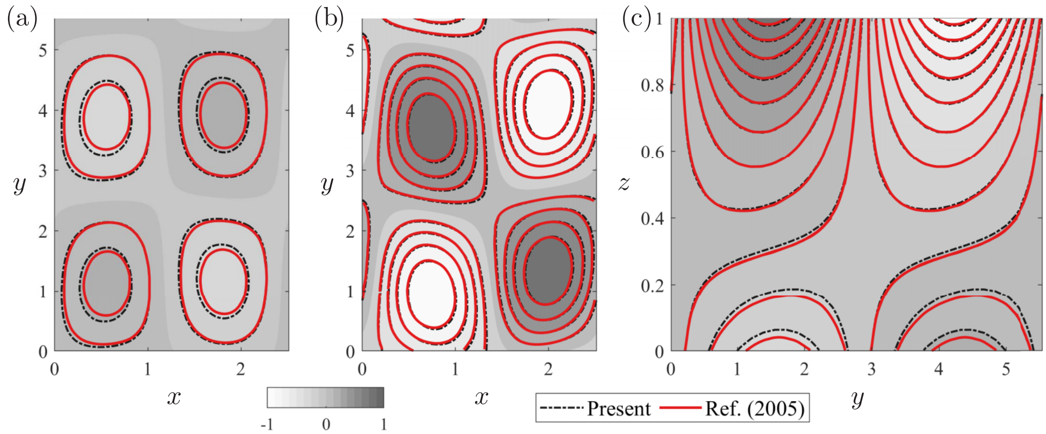

FIG. 20. Contours of the perturbation temperature (counterpart of buoyancy) of the first Floquet mode: horizontal sections at the (a) bottom and (b) surface, and (c) the y-z section at $x = 1.78$. The reference data are from Stevens and Hakim [56].

APPENDIX C: THE PRIMITIVE EQUATION MODEL

The linearized PEs used in Sec. III are written as

$$
\begin{aligned}
&\mathrm{Ro}\left(\frac{\partial}{\partial t} + V_B\frac{\partial}{\partial y}\right)u' - fv' + \frac{\partial p'}{\partial x} = -r_R u' + \mathscr{D}_u,\\
&\mathrm{Ro}\left(\frac{\partial}{\partial t} + V_B\frac{\partial}{\partial y}\right)v' + fu' + \mathrm{Fr}^2 V_{B,z}w' + \frac{\partial p'}{\partial y} = -r_R v' + \mathscr{D}_v,\\
&\frac{\partial p'}{\partial z} = b',\\
&\left(\frac{\partial}{\partial t} + V_B\frac{\partial}{\partial y}\right)b' + fV_{B,z}u' + N^2 w' = -r_R b' + \mathscr{D}_b,\\
&\frac{\partial u'}{\partial x} + \frac{\partial v'}{\partial z} + \frac{\mathrm{Fr}^2}{\mathrm{Ro}}\frac{\partial w'}{\partial z} = 0,
\end{aligned}
\tag{C1}
$$

where the dissipative terms $\mathscr{D}_u$, $\mathscr{D}_v$, and $\mathscr{D}_b$ are formulated as in Sec. II A. Equation (C1) is discretized on a staggered mesh for well-posedness, following Molemaker *et al.* [68]. The perturbation energy norm for the PE model required in TGA is the same as Eq. (10). Verification of the PE solver can be found in the authors' previous work [42].

[1] C. Wunsch and R. Ferrari, Vertical mixing, energy, and the general circulation of the oceans, Annu. Rev. Fluid Mech. **36**, 281 (2004).
[2] R. Pierrehumbert and K. Swanson, Baroclinic instability, Annu. Rev. Fluid Mech. **27**, 419 (1995).
[3] J. Charney and M. Stern, On the stability of internal baroclinic jets in a rotating atmosphere, J. Atmos. Sci. **19**, 159 (1962).
[4] J. Pedlosky, The stability of currents in the atmosphere and the ocean: Part I, J. Atmos. Sci. **21**, 201 (1964).
[5] K. Smith, The geography of linear baroclinic instability in Earth's oceans, J. Mar. Res. **65**, 655 (2007).

[6] L. Feng, C. Liu, A. Köhl, D. Stammer, and F. Wang, Four types of baroclinic instability waves in the global oceans and the implications for the vertical structure of mesoscale eddies, J. Geophys. Res.: Oceans **126**, e2020JC016966 (2021).
[7] N. Phillips, Energy transformations and meridional circulations associated with simple baroclinic waves in a two-level, quasi-geostrophic model, Tellus **6**, 274 (1954).
[8] D. Chelton, M. Schlax, and R. Samelson, Global observations of nonlinear mesoscale eddies, Prog. Oceanogr. **91**, 167 (2011).
[9] J. Pedlosky, Finite-amplitude baroclinic waves, J. Atmos. Sci. **27**, 15 (1970).
[10] J. Pedlosky, The nonlinear dynamics of baroclinic wave ensembles, J. Fluid Mech. **102**, 169 (1981).
[11] J. Hart, Wavenumber selection in nonlinear baroclinic instability, J. Atmos. Sci. **38**, 400 (1981).
[12] P. Klein and J. Pedlosky, A numerical study of baroclinic instability at large supercriticality, J. Atmos. Sci. **43**, 1243 (1986).
[13] A. Simmons and B. Hoskins, The life cycles of some nonlinear baroclinic waves, J. Atmos. Sci. **35**, 414 (1978).
[14] J. G. Charney and J. G. DeVore, Multiple flow equilibria in the atmosphere and blocking, J. Atmos. Sci. **36**, 1205 (1979).
[15] M. Ikeda, Meanders and detached eddies of a strong eastward-flowing jet using a two-layer quasi-geostrophic model, J. Phys. Oceanogr. **11**, 526 (1981).
[16] J. Wang and M. Ikeda, Diagnosing ocean unstable baroclinic waves and meanders using the quasi-geostrophic equations and Q-vector method, J. Phys. Oceanogr. **27**, 1158 (1997).
[17] D. Hansen, Gulf Stream meanders between Cape Hatteras and the Grand Banks, Deep Sea Res. **17**, 495 (1970).
[18] M. Spall and A. Robinson, Regional primitive equation studies of the Gulf Stream meander and ring formation region, J. Phys. Oceanogr. **20**, 985 (1990).
[19] G. Sutyrin, I. Ginis, and S. Frolov, Equilibration of baroclinic meanders and deep eddies in a Gulf Stream-type jet over a sloping bottom, J. Phys. Oceanogr. **31**, 2049 (2001).
[20] M. Youngs, A. Thompson, A. Lazar, and K. Richards, ACC meanders, energy transfer, and mixed barotropic-baroclinic instability, J. Phys. Oceanogr. **47**, 1291 (2017).
[21] T. Waseda, H. Mitsudera, B. Taguchi, and Y. Yoshikawa, On the eddy-Kuroshio interaction: Meander formation process, J. Geophys. Res.: Oceans **108**, 2002JC001583 (2003).
[22] I. da Silveira, J. Lima, A. Schmidt, W. Ceccopieri, A. Sartori, C. Franscisco, and R. Fontes, Is the meander growth in the Brazil current system off southeast Brazil due to baroclinic instability, Dyn. Atmos. Oceans **45**, 187 (2008).
[23] I. Orlanski and M. Cox, Baroclinic instability in ocean currents, Geophys. Fluid Dyn. **4**, 297 (1973).
[24] T. Simons, The nonlinear dynamics of cyclone waves, J. Atmos. Sci. **29**, 38 (1972).
[25] R. Panetta, Zonal jets in wide baroclinically unstable regions: Persistence and scale selection, J. Atmos. Sci. **50**, 2073 (1993).
[26] J. Pedlosky, On secondary baroclinic instability and the meridional scale of motion in the ocean, J. Phys. Oceanogr. **5**, 603 (1975).
[27] G. Moore and W. Peltier, Nonseparable baroclinic instability. Part I: Quasi-geostrophic dynamics, J. Atmos. Sci. **46**, 57 (1989).
[28] V. Theofilis, Global linear instability, Annu. Rev. Fluid Mech. **43**, 319 (2011).
[29] K. Donohue, D. Watts, P. Hamilton, R. Leben, and M. Kennelly, Loop current eddy formation and baroclinic instability, Dyn. Atmos. Oceans **76**, 195 (2016).
[30] J. Li and J. Gan, Characteristics and formation of the Luzon undercurrent in the western north pacific: Observational study, J. Geophys. Res.: Oceans **127**, e2022JC018968 (2022).
[31] X. Chen, J. Gan, C. Hui, and J. McWilliams, Parameterization of the vertical mixing for the Luzon Undercurrent in the northern western pacific ocean (unpublished).
[32] www.hycom.org
[33] J. Gan, Z. Liu, and C. Hui, A three-layer alternating spinning circulation in the South China Sea, J. Phys. Oceanogr. **46**, 2309 (2016).

[34] J. Gan, H. Kung, Z. Cai, Z. Liu, C. Hui, and J. Li, Hotspots of the Stokes rotating circulation in a large marginal sea, Nat. Commun. **13**, 2223 (2022).
[35] P. Stone, On non-geostrophic baroclinic stability: Part II, J. Atmos. Sci. **27**, 721 (1970).
[36] A. Robinson, M. Spall, and N. Pinardi, Gulf Stream simulations and the dynamics of ring and meander processes, J. Phys. Oceanogr. **18**, 1811 (1988).
[37] P. Berloff, I. Kamenkovich, and J. Pedlosky, A model of multiple zonal jets in the oceans: Dynamical and kinematical analysis, J. Phys. Oceanogr. **39**, 2711 (2009).
[38] G. Roullet, J. McWilliams, X. Capet, and M. Molemaker, Properties of steady geostrophic turbulence with isopycnal outcropping, J. Phys. Oceanogr. **42**, 18 (2012).
[39] P. Klein, B. Hua, G. Lapeyre, X. Capet, S. Le Gentil, and H. Sasaki, Upper ocean turbulence from high-resolution 3D simulations, J. Phys. Oceanogr. **38**, 1748 (2008).
[40] P. Zurita-Gotor and G. Vallis, Equilibration of baroclinic turbulence in primitive equations and quasi-geostrophic models, J. Atmos. Sci. **66**, 837 (2009).
[41] J. Pedlosky and J. Thomson, Baroclinic instability of time-dependent currents, J. Fluid Mech. **490**, 189 (2003).
[42] X. Chen, J. Gan, and J. C. McWilliams, Biglobal analysis of baroclinic instability in a current-undercurrent oceanic system, Phys. Rev. Fluids **8**, 123801 (2023).
[43] B. Farrell and P. Ioannou, Generalized stability theory. Part I: Autonomous operators, J. Atmos. Sci. **53**, 2025 (1996).
[44] T. Radko, D. de Carvalho, and J. Flanagan, Nonlinear equilibration of baroclinic instability: The growth rate balance model, J. Phys. Oceanogr. **44**, 1919 (2014).
[45] T. Herbert, Parabolized stability equations, Annu. Rev. Fluid Mech. **29**, 245 (1997).
[46] P. Paredes, M. Hermanns, S. Le Clainche, and V. Theofilis, Order 10^4 speedup in global linear instability analysis using matrix formation, Comput. Methods Appl. Mech. Eng. **253**, 287 (2013).
[47] L. Zhao, C. Zhang, J. Liu, and J. Luo, Improved algorithm for solving nonlinear parabolized stability equations, Chin. Phys. B **25**, 084701 (2016).
[48] K. J. Burns, G. M. Vasil, J. S. Oishi, D. Lecoanet, and B. P. Brown, Dedalus: A flexible framework for numerical simulations with spectral methods, Phys. Rev. Res. **2**, 023068 (2020).
[49] P. Berloff, I. Kamenkovich, and J. Pedlosky, A mechanism of formation of multiple zonal jets in the oceans, J. Fluid Mech. **628**, 395 (2009).
[50] J. Taylor and R. Ferrari, On the equilibration of a symmetrically unstable front via a secondary shear instability, J. Fluid Mech. **622**, 103 (2009).
[51] X. Chen, Y. Xi, J. Ren, and S. Fu, Cross-flow vortices and their secondary instabilities in hypersonic and high-enthalpy boundary layers, J. Fluid Mech. **947**, A25 (2022).
[52] J. Hilditch and L. Thomas, Parametric subharmonic instability of inertial shear at ocean fronts, J. Fluid Mech. **966**, A34 (2023).
[53] T. Herbert, Secondary instability of boundary layers, Annu. Rev. Fluid Mech. **20**, 487 (1988).
[54] C. Wolfe and R. Samelson, Normal-mode analysis of a baroclinic wave-mean oscillation, J. Atmos. Sci. **63**, 2795 (2006).
[55] I. Shevchenko, P. Berloff, D. Guerrero-López, and J. Roman, On low-frequency variability of the midlatitude ocean gyres, J. Fluid Mech. **795**, 423 (2016).
[56] G. Stewart, A Krylov–Schur algorithm for large eigenproblems, SIAM J. Matrix Anal. Appl. **23**, 601 (2002).
[57] M. Stevens and G. Hakim, Perturbation growth in baroclinic waves, J. Atmos. Sci. **62**, 2847 (2005).
[58] X. Chen, L. Wang, and S. Fu, Energy transfer of hypersonic and high-enthalpy boundary layer instabilities and transition, Phys. Rev. Fluids **7**, 033901 (2022).
[59] V. Zemskova, P.-Y. Passaggia, and B. White, Transient energy growth in the ageostrophic Eady model, J. Fluid Mech. **885**, A29 (2020).
[60] E. Heifetz and B. Farrell, Generalized stability of nongeostrophic baroclinic shear flow. Part I: Large Richardson number regime, J. Atmos. Sci. **60**, 2083 (2003).
[61] J. McWilliams and J. Chow, Equilibrium geostrophic turbulence I: A reference solution in a β-plane channel, J. Phys. Oceanogr. **11**, 921 (1981).

[62] X. Wu and P. Stewart, Interaction of phase-locked modes: A new mechanism for the rapid growth of three-dimensional disturbances, J. Fluid Mech. **316**, 335 (1996).
[63] N. Nakamura, Momentum flux, flow symmetry, and the nonlinear barotropic governor, J. Atmos. Sci. **50**, 2159 (1993).
[64] P. Gent and J. McWilliams, Isopycnal mixing in ocean circulation models, J. Phys. Oceanogr. **20**, 150 (1990).
[65] G. Moore and W. Peltier, Cyclogenesis in frontal zones, J. Atmos. Sci. **44**, 384 (1987).
[66] V. Gushchin and A. Fedorov, Excitation and development of unstable disturbances in a supersonic boundary layer, Fluid Dyn. **25**, 344 (1990).
[67] L. Thomas and J. Taylor, Damping of inertial motions by parametric subharmonic instability in baroclinic currents, J. Fluid Mech. **743**, 280 (2014).
[68] M. Molemaker, J. McWilliams, and I. Yavneh, Baroclinic instability and loss of balance, J. Phys. Oceanogr. **35**, 1505 (2005).